Morphodynamic impacts of large-scale engineering projects in the Yangtze River delta

Luan, Hualong; Ding, P; Wang, Zhengbing ; Yang, S.L.; Lu, Jin You

DOI
10.1016/j.coastaleng.2018.08.013

Publication date
2018

Document Version
Accepted author manuscript

Published in
Coastal Engineering

Morphodynamic impacts of large-scale engineering projects in the Yangtze River delta

Hua Long Luan [a], Ping Xing Ding [a, *], Zheng Bing Wang [a, b, c], Shi Lun Yang [a], Jin You Lu[a]

[a] State Key Laboratory of Estuarine and Coastal Research, East China Normal University, Shanghai 200062, China

[b] Faculty of Civil Engineering and Geosciences, Delft University of Technology, P.O. Box 5048, 2600 GA Delft, The Netherlands

[c] Deltares, P.O. Box 177, 2600 MH Delft, The Netherlands

*Corresponding author.

Tel: +86 021-62232897

Fax: +86 021-62233468

E-mail address: pxding@sklec.ecnu.edu.cn (Prof. P.X. Ding)

Highlights

- ✓ The seaward part of the mouth bar area converted from accretion to overall erosion along with river sediment reduction since 1997.
- ✓ Morphodynamics of the mouth bar area since 1997 show distinct spatiotemporal variations.
- ✓ The training walls along the North Passage significantly modified the hydrodynamics in the mouth bar area.
- ✓ The downstream half of the north dike contributed to the accretion at the East Hengsha Shoal and erosion at seaward end of the North and South Passage.

Abstract

Impacts of local human interventions on morphodynamics of large river deltas are insufficiently understood, especially superimposed upon delta erosion due to diminishing sediment supplies. The densely populated Yangtze Estuary in China is increasingly influenced by large-scale estuarine engineering projects in the recent two decades and thereby provides a useful example to address this issue. This work investigates the morphological impacts of the Deepwater Navigation Channel Project (DNCP) including dikes and groynes implemented in 1997-2010 on the mouth bar area of the Yangtze Estuary through data analysis and process-based modeling approach (Delft3D). The seaward portion of the mouth bar area, defined as the study area for calculation of sediment volume change, converted from net accretion to net erosion during 1997-2013 primarily due to river sediment reduction. However, the East Hengsha Shoal (EHS) showed abnormal accretion in the same period. The accretion-erosion conversion occurred around the year 2004 is largely contributed by two erosion zones at the northern and southern subaqueous delta, respectively. Hydrodynamic simulations indicate that the training walls result in weaker tidal flow and longer slack period at the EHS and stronger tidal flow at the southern erosion zone. Subsequently, morphological modeling demonstrates that the training walls enhance accretion at the EHS, which is mainly attributed to the downstream half of the north dike. This can be verified by the consistent period (2002-2004) of the dike extension to the present location and accretion peak of the EHS. Morphological modeling also indicates that the downstream half of the north dike enhanced erosion at the southern erosion zone, which can partly explain the gradual increase in the erosion volume of both erosion zones after 2004. Under large-scale estuarine

engineering projects, the Yangtze subaqueous delta is accelerating to approach morphodynamic equilibrium. The timescale to the erosion limit and sustainable estuarine management merit further systematic research.

Keywords: Morphodynamics; River sediment reduction; Estuarine engineering projects; Mouth bar area; Yangtze Estuary

1. Introduction

Modern deltas across the globe, originated since the maximum Holocene transgression (Stanley and Warne, 1994), are actively propagating systems as redundant fluvial sediment accumulated hereon after part of the amount being taken away by marine currents (Coleman and Wright, 1975; Syvitski and Saito, 2007). Anthropogenic activities in drainage basins strongly modified such propagation processes by increasing sediment productions over the past millennia and decreasing sediment loads in the past century (Milliman et al., 1987; Hori et al., 2001; Syvitski et al., 2005). Though the definition of the Anthropocene in the geological sense is controversial (Syvitski and Kettner, 2011; Renaud et al., 2013), there is no doubt that morphodynamics of world's deltas are altering from natural evolution driven to anthropogenic impact driven (Syvitski and Saito, 2007). Engineering controls within deltaic plains, particularly in the recent decades, are likely to accelerate the alteration process superimposed upon the effect of low sediment supply due to upstream dam construction and improved soil conservation (Vörösmarty et al., 2003; Walling, 2006). Therefore, it is urgently needed to strengthen our understanding on the morphodynamics of these dynamic and vulnerable environments, regarding that deltas are home to more than half a billion people and thousands of plant and animal species (Giosan et al., 2014), and thereby hold high ecological and socio-economic value (Day et al., 1989).

The fluvial sediment reduction compounded with rising seas has resulted in delta erosion and flooding around the world (Ericson et al., 2006; Syvitski et al., 2009). The close link between human-induced decrease of sediment loads and delta erosion is identified by numerous case studies on large deltas, including the Nile (Stanley, 1996), Mississippi (Blum

and Roberts, 2009), Ebro (Sanchez-Arcilla et al., 1998), Mekong (Anthony et al., 2015), and Yellow (Chu et al., 2006; Wang et al., 2007). Most densely populated deltas were further interfered by vicinal human interventions. The Mississippi River Delta, for instance, is suffering from rapid subsidence and land loss caused by intensive hydrocarbon extraction (Morton et al., 2005). Flow path control of distributary channels also produced remarkable impacts on delta evolution as occurred in Colorado, Po and Yellow deltas (Syvitski and Saito, 2007). Other local interventions include training wall construction, dredging, reclamation, etc. (Blott et al., 2006; Wu et al., 2016). Rapid urbanization and resource utilization within deltaic areas are likely to aggravate the risk and sustainability of deltas (Syvitski, 2008).

The Yangtze River delta in China provides a useful example to examine deltaic morphodynamics under human interventions because this large-scale and densely populated delta is heavily impacted by human activities from both the upstream reach and deltaic region (Fig. 1a) (De Vriend et al., 2011). Many estuarine engineering projects have been conducted in the recent 2 decades for navigation, flood control, freshwater consumption and wetland management purposes (Tian et al., 2015; Luan et al., 2016). Present study concentrates on the mouth bar area and adjacent part of the subaqueous delta spanning from the East Hengsha Shoal (EHS) and Jiuduansha Shoal (JS) to the isobath of nearly 30 m (Fig. 1b), which have been significantly interfered by estuarine engineering projects since 1997 (Luan et al., 2016).

Under decreasing river sediment supply after the constructions of more than 50,000 dams throughout the watershed (Yang et al., 2011), multiple evidences for overall delta erosion have been identified in terms of bed level changes (Yang et al., 2011), grain size variations (Luo et al., 2017), sediment transport capacity of coastal currents (Deng et al., 2017)

97 and isotopic tracing (Wang et al., 2017). Dai et al. (2014) reported that the Yangtze
98 subaqueous delta rebounded from slight erosion to high accumulation with much higher
99 accumulation amount than river sediment supply after the operation of the Three Gorge Dam
100 (TGD) in 2003, whereas the sources of the excess sediment and relevant processes for
101 sediment re-distribution remained unknown. Zhu et al. (2016) demonstrated that the recent
102 erosion of the subaqueous delta can be related to the training walls along the North Passage
103 which significantly modified the estuarine hydrodynamics as suggested by a model-based
104 study. Luan et al. (2016) found that the northern part of the mouth bar area, particularly the
105 EHS, converted from net erosion in 1986-1997 to net accretion in 1997-2010. The mouth bar
106 area in the latter period showed slightly net accretion though simultaneous erosion in its
107 southern part was observed. However, Luan et al. (2016) only provided the morphological
108 difference of the mouth bar area before and after the constructions of training walls. Neither
109 the evolution processes within the period (1997-2010) nor the physical mechanisms
110 responsible for the enhanced accretion at the EHS were investigated. Furthermore, the
111 separated influences of estuarine human interventions and river sediment reduction on
112 morphological changes are still less understood. Therefore, this study combines bathymetric
113 data analysis and process-based modeling approach (Delft3D) to examine the morphological
114 evolution and mechanisms of the mouth bar area under large-scale estuarine engineering
115 projects since 1997. The results should be valuable for sustainable management of the
116 Yangtze Estuary and other densely populated river deltas in the world.
117
118 **2. Study area**

The Yangtze River, ranking the largest and longest in Asia (Milliman and Farnsworth, 2013), reaches its end near Shanghai City and enters the inner shelf of the East China Sea (Fig. 1a). Abundant river sediment supply contributed to rapid delta progradation with approximately 50 km per millennium since the mid-Holocene (Hori et al., 2001). Currently, the Yangtze subaqueous delta covers an area of over 10,000 km^2 spanning from the crest of the mouth bar to the paleo-incised valley (30-50 m) (Chen et al., 1985). The seabed at the mouth bar area is dominated by fine cohesive mud which can be frequently resuspended by tidal currents (Liu et al., 2010; Luo et al., 2012). This area behaves as both the estuarine turbidity maximum and depocenter of the delta (Chen et al., 1985; Dai et al., 2014). Mean tidal range and wave height at the mouth is 2.67 m and 0.9 m, respectively (Yun, 2004). Meanwhile, the delta receives huge amount of river inputs from the upstream river, i.e. 896 km^3/yr of runoff and 390 Mt/yr of suspended sediment load in 1950-2010 (CWRC, 2011). Under combined large river flow, meso-tidal and minor wave forcing, the Yangtze River delta is defined as a mixed river- and tidal-dominant mud delta and featured by a funnel-shaped topography with wide distributary channels and accreting intertidal flats (Fig. 1b).

No significant variation trend was observed for the annual water runoff in the past half century, while the annual sediment load remained at a high level in the 1950-1960s and decreased continuously after the 1980s (Fig. 2). The decreasing trend was accelerated since the late 1990s and gradually vanished after the closure of the TGD in 2003 (Fig. 2). The sediment load retained at a relatively low level in the post-TGD decade (145 Mt/yr) which is only about 30% of that in 1950-1968 (Yang et al., 2015). Notably, the sediment load was as low as 85 Mt/yr and 72 Mt/yr in the extreme drought year 2006 and 2011, respectively (Fig.

141 2).

142 Under the condition of low sediment supply in the recent 2 decades, many engineering
143 projects have been constructed within the estuarine area. One of the largest in the study area is
144 the Deep Navigation Channel Project (DNCP) along the North Passage (Fig. 1b) which was
145 aimed at improving the navigational capacity. The DNCP was implemented through three
146 phases from 1998 to 2010 including constructions of training walls and intensive dredging.
147 The upstream and downstream parts of the dikes and groynes were constructed in Phase I
148 (1998.01-2002.06) and Phase II (2002.05-2004.12), respectively, resulting in 100.7 km as the
149 total length of the twin dikes and 19 perpendicular groynes (Fig. 1c). The bathymetry within
150 the North Passage responded rapidly to the constructions of training walls through severe
151 deposition in the dike-sheltered areas and siltation in the navigational channel (Liu et al.,
152 2011; Dai et al., 2013). Phase III (2006.09-2010.03) of the project mainly includes the
153 construction of submerged dikes in the south side, groyne extensions and dredging (Fig. 1c).
154 As a consequence, the deep navigation channel between the north and south dike was
155 deepened from 6.5 m before the project in 1998 to 8.5 m in 2001, 10 m in 2005 and 12.5 m in
156 2011. Thus, the mouth bar in the North Passage was broken through after a plenty of dredging
157 efforts. Other engineering projects within the mouth bar area include the land reclamation at
158 EHS and East Nanhui Mudflat, which also heavily impacted the morphological evolution of
159 the Yangtze Estuary (Wei et al., 2015).

160

161 **3. Method**

3.1 Data collection and processing

To assess the morphological processes during estuarine engineering projects, we collected navigational charts and bathymetric maps based on observations in various years (1997, 2002, 2004, 2007, 2010 and 2013) which captured each phase of the DNCP (Tab. S1). An echo sounder and a global positioning system (Trimble Navigation Limited, California, USA) were used for depth measurements and position recordings, respectively, with vertical and horizontal errors of 0.1 m and 1 m. In line with the analyzing procedure by Luan et al. (2016), the depth points digitized from navigational charts are combined with bathymetric maps to cover the whole mouth bar area and adjacent part of subaqueous delta (Fig. S1). The scales of the maps range from 1:50,000 to 1:130,000 (Tab. S1), and the averaged data density ranges from 1.1 to 11.5 samples/km^2 which is sufficiently high for calculation of morphological evolution with acceptable accuracy (Dai et al., 2014; Luo et al., 2017). Depth points of each year, referenced to the theoretical lowest-tide datum at Wusong, are interpolated into a 50×50 m grid by the Kriging interpolation technique in the Surfer mapping software package. Consequently, a digital elevation model (DEM) is generated for each year of bathymetric data (Fig. 3a1-f1). The erosion/deposition patterns are obtained by subtracting a later DEM from an earlier one (Fig. 3a2-e2). We assume that the dominant cause for water depth variation is bed sediment erosion and deposition (Yang et al., 2011; Dai et al., 2013, 2014). Inspired by Yang et al. (2011) and Zhu et al. (2016), a rectangle domain covering seaward of the mouth bar area and adjacent part of the subaqueous delta is chosen for erosion/deposition calculations. The North Passage and the dredged navigation channel are excluded from the study area as this study aims at exploring training-wall-induced

bathymetric changes of the mouth bar area beyond the North Passage (Fig. 1b). In order to investigate the spatial differences of the morphological changes, the study area are firstly divided into a northern part and a southern part by an eastward extending line of the northern dike. The 10m-isobath in 1997 is used to further separate the two parts into four sub-areas in total, i.e. Areas N1, N2, S1 and S2 (

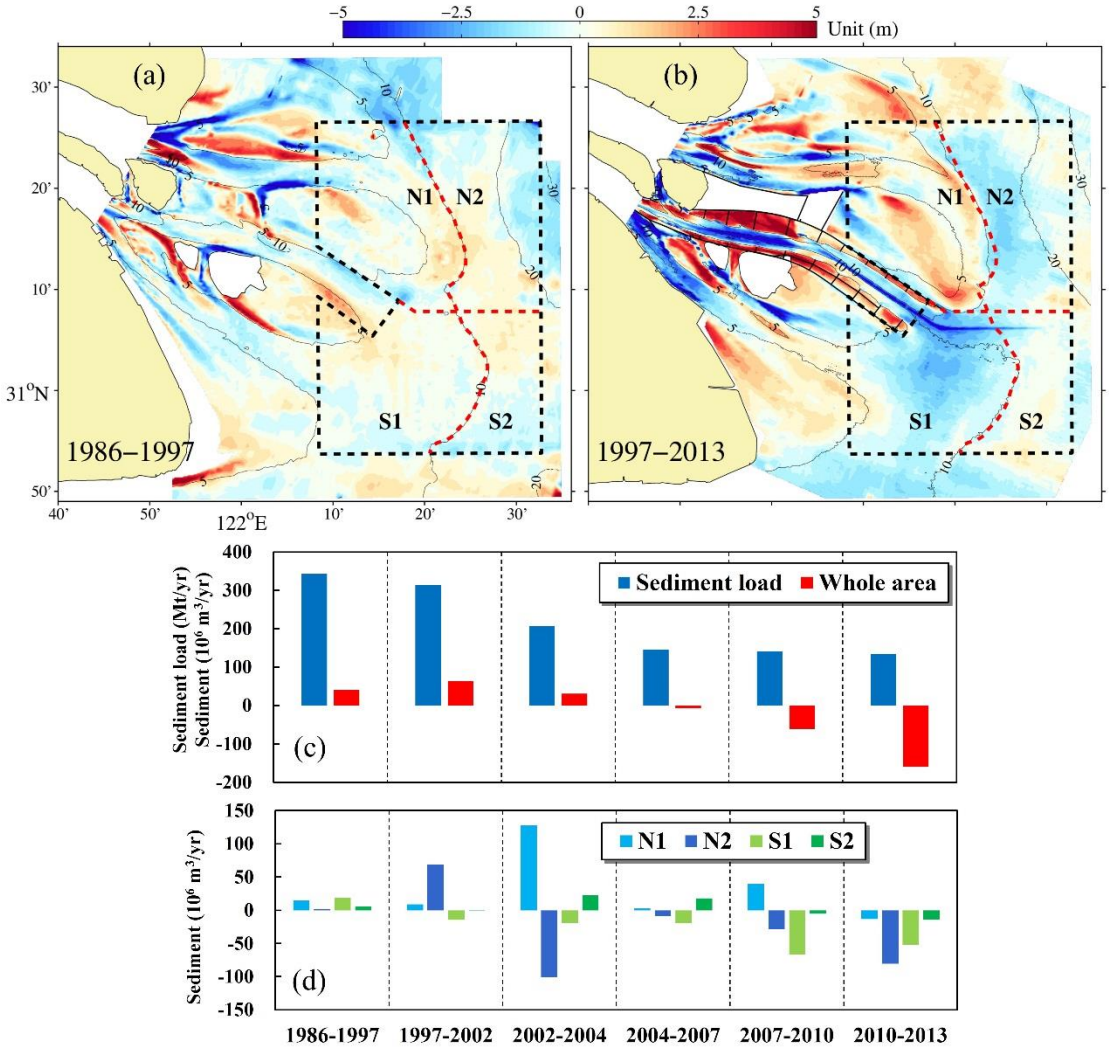

Fig. 4a). The erosion/deposition area percentages, yearly sediment volume changes and net changes of the whole study area and four sub-areas are calculated based on the bed-level changes, grid resolution, domain areas and year spans (Luan et al., 2016)

194 (

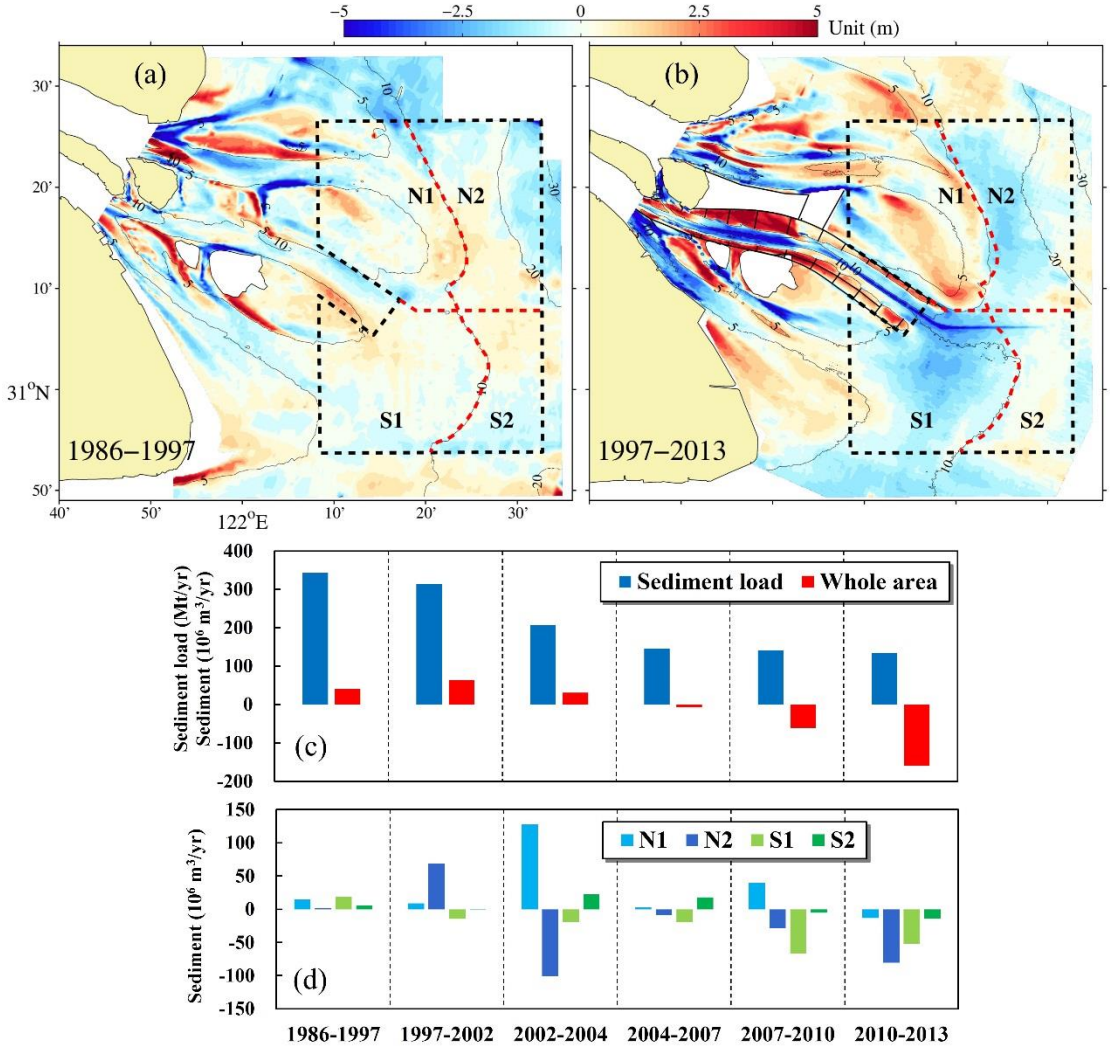

195

196 Fig. 4c, d; Tab. S2, S3). Three typical sections in the study area (Fig. 5) are extracted

197 from the DEM to describe the amplitudes of bed-level changes.

198 3.2 Process-based morphological modeling

199 The process-based Delft3D model system is applied to examine the impacts of training

200 walls on hydrodynamics and morphological changes. The model solves shallow water

201 equations under hydrostatic pressure assumption in a horizontal curvilinear grid and is fully

202 integrated with hydrodynamic, sediment transport and morphological updating modules

203 (Lesser et al., 2004). Medium- to long-term morphodynamic modeling can be implemented

204 through linearly accelerating bed-level change each hydrodynamic time step with a carefully
205 selected morphological factor (MF) (Roelvink, 2006). Thus, the model online couples flow
206 and morphology and produces bathymetric change in an up-scaled period. Numerous case
207 studies have demonstrated high capacity of the Delft3D model system on reproducing
208 detailed flow features, sediment dynamics and morphological evolution of coastal and
209 estuarine systems (van der Wegen et al., 2011; Dissanayake et al., 2012; van Maren et al.,
210 2015; Su et al., 2016; Luan et al., 2017).

211 The morphological model of the Yangtze Estuary applied in this study considers tidal
212 forcing, river discharge, wind wave, sediment transport and online bed-level change.
213 Variations in river inputs and multiple sediment fractions (cohesive and noon-cohesive) are
214 included in the model due to strong river seasonality and highly graded bed sediment within
215 the estuarine area. Promising hindcasting of the decadal morphodynamic evolution of the
216 Yangtze Estuary were carried out for three historical periods involving distinct morphological
217 processes, a rapid accretion period (1958-1978), an erosional period (1986-1997) and a recent
218 period with slight accretion (2002-2010). Details of the model setup and hindcast results were
219 described by Luan et al. (2017). Hindcast case of the recent period which corresponds to the
220 constructing period of the DNCP shows best model performance and thereby provides a nice
221 reference case for investigating impacts of training walls on hydrodynamics and
222 morphological evolution. One numerical experiment is firstly conducted which excludes all
223 the dikes and groynes along the North Passage from the reference case to explore the overall
224 impacts of the training walls. The northern and southern dikes were extended to the present
225 location after the Phase II of the DNCP and induced severe siltation in the middle of the

dredged channel (Liu et al., 2011). Dikes implemented in Phase II are close to the EHS and the observed erosion zones at the subaqueous delta (Luan et al., 2016; Zhu et al., 2016). Therefore, two further numerical experiments are conducted which exclude the downstream half of the northern and southern structures from the reference case, respectively. The modeled hydrodynamics, sediment transport processes and subsequent bed-level changes in the above three experiments are compared with the reference case to provide physical explanations of the observed evolution under large-scale estuarine engineering projects.

4. Results

4.1 Morphological changes during 1997-2013

The erosion/deposition patterns during 1997-2013 show distinct spatial variations, reflected by accretion at the EHS and erosion at the seaward end of the North and South Passage

(

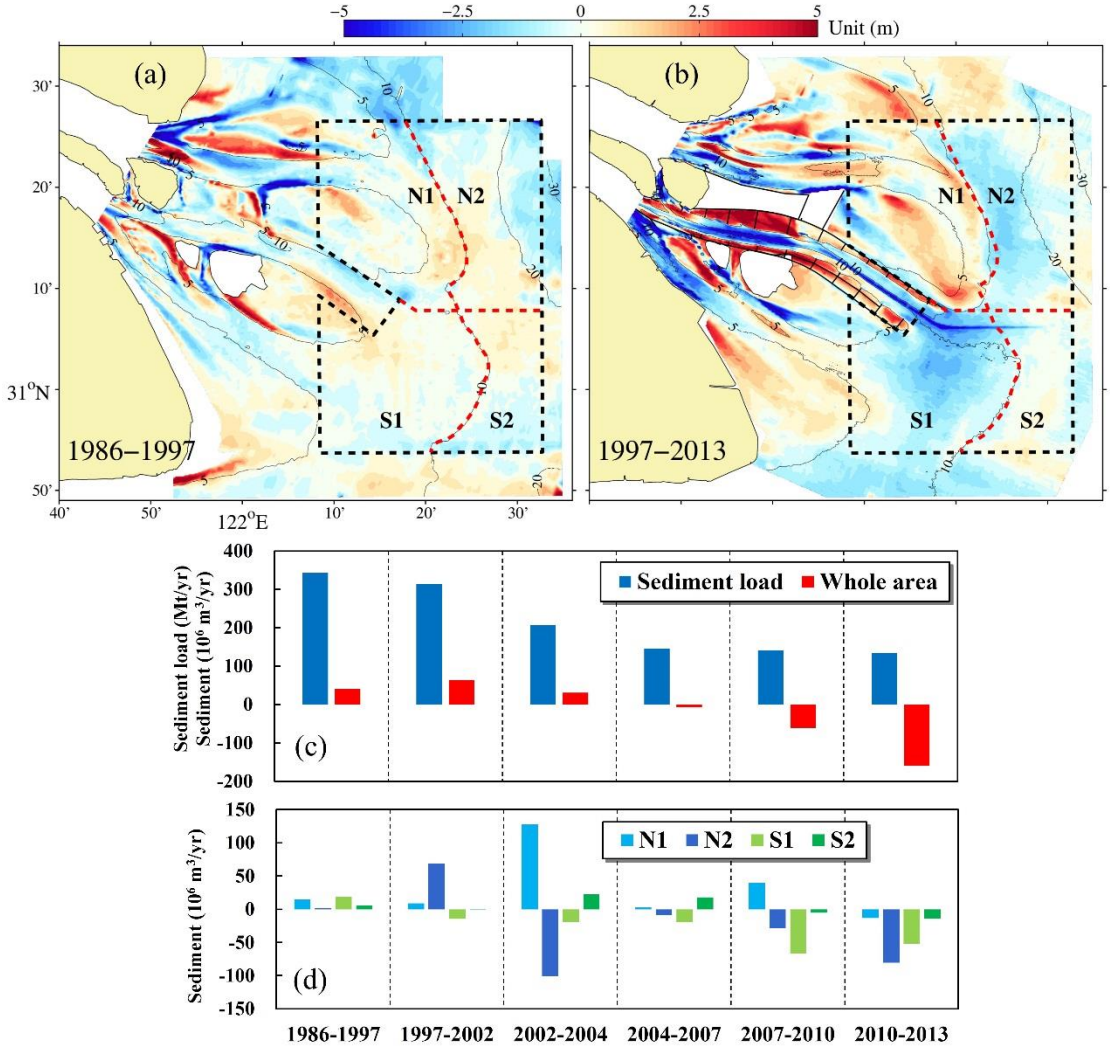

240

241 Fig. 4b). For the comparison purpose, the pattern in 1986-1997 is also presented

242 (

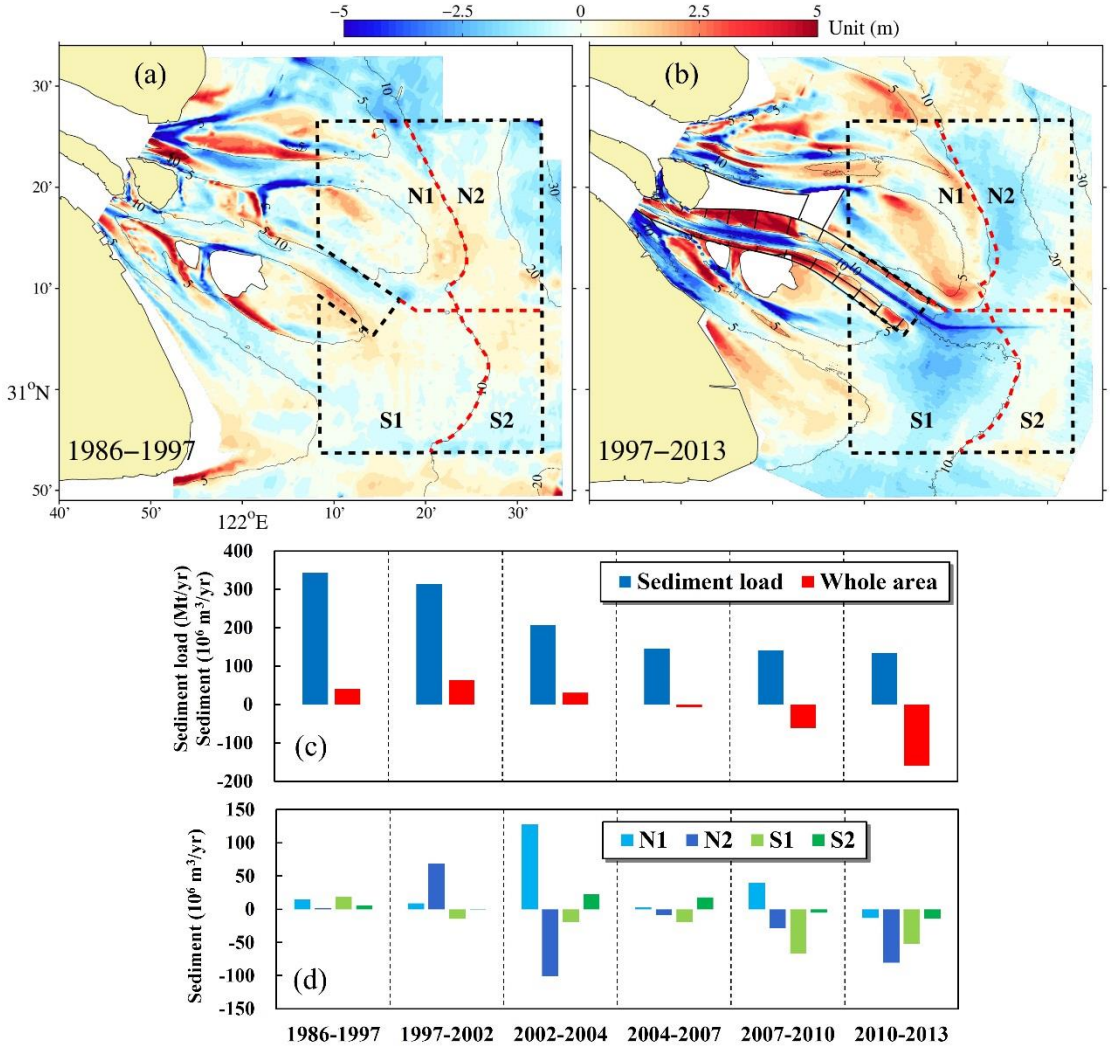

Fig. 4a). The latter area involved strong deposition in 1986-1997 as higher river sediment discharge fed the delta. On the contrary, accretion at the EHS increased from 1986-1997 to 1997-2013 under decreased sediment supply. In addition to similar descriptions by Zhu et al. (2016), the morphological evolution processes in shorter intervals (2-5 years) within the period (1997-2013) are presented (Fig. 3a2-e2). The patterns indicate that continuous erosion occurred at the seaward end of North and South Passage since 1997, while accretion at the EHS peaked in 2002-2004 and decreased after 2004 (Fig. 3b2). The deep part (>10 m) of the northern subaqueous delta converted from deposition to erosion around the year 2002 and showed continuous erosion in 2002-2013. The deep part (>10 m) of the

253 southern subaqueous delta experienced episodic deposition and erosion in the study period. In
254 2010-2013, the mouth bar area and adjacent part of the subaqueous delta were dominated by
255 overall erosion (Fig. 3e2).

256 Sediment volume changes provide quantitative assessment of morphological evolution.
257 As shown in the

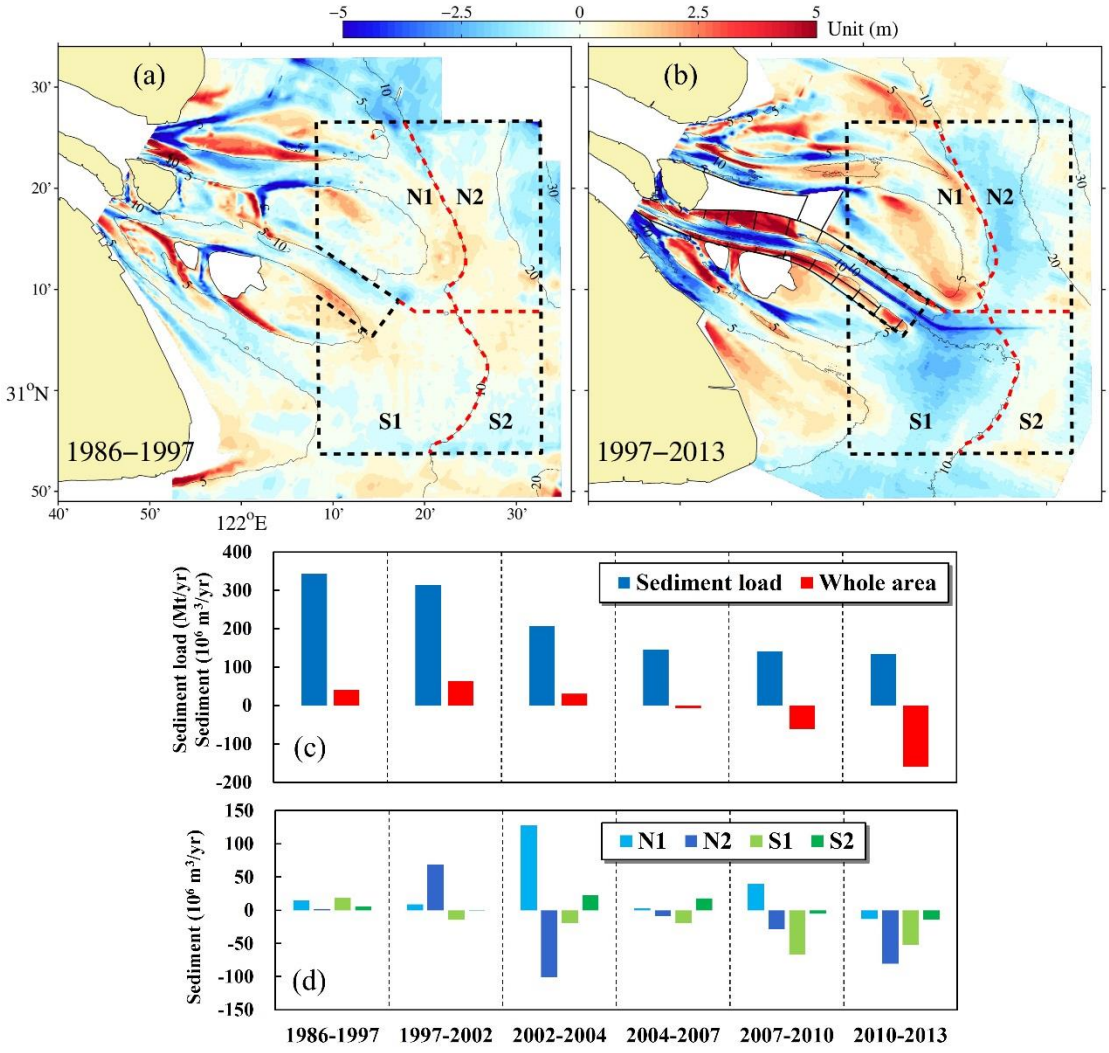

258

259 Fig. 4c, a coherent conversion from net accretion to erosion of the whole study area
260 occurred around the year 2004 along with the decreasing sediment supply. The net accretion
261 volume increased from 40.6 Mm^3/yr in 1986-1997 to 63.6 Mm^3/yr in 1997-2002, possibly due
262 to much longer time span of the earlier period and thereby bed sediment compaction during

the same period. The sediment discharge decreased from 251 Mm^3/yr in 1997-2002 to 117 Mm^3/yr in 2004-2007, and the decreasing rate slowed down significantly in the later two periods, i.e. 113 Mm^3/yr in 2007-2010 and 107 Mm^3/yr in 2010-2013 (Tab. S2). However, the net erosion amount showed almost linear increase from −7.0 $Mm^3\ yr^{-1}$ in 2004-2007 to −159.6 $Mm^3\ yr^{-1}$ in the latest period, and the net erosion rate reached as high as −71.8 mm yr^{-1} in the latest period (

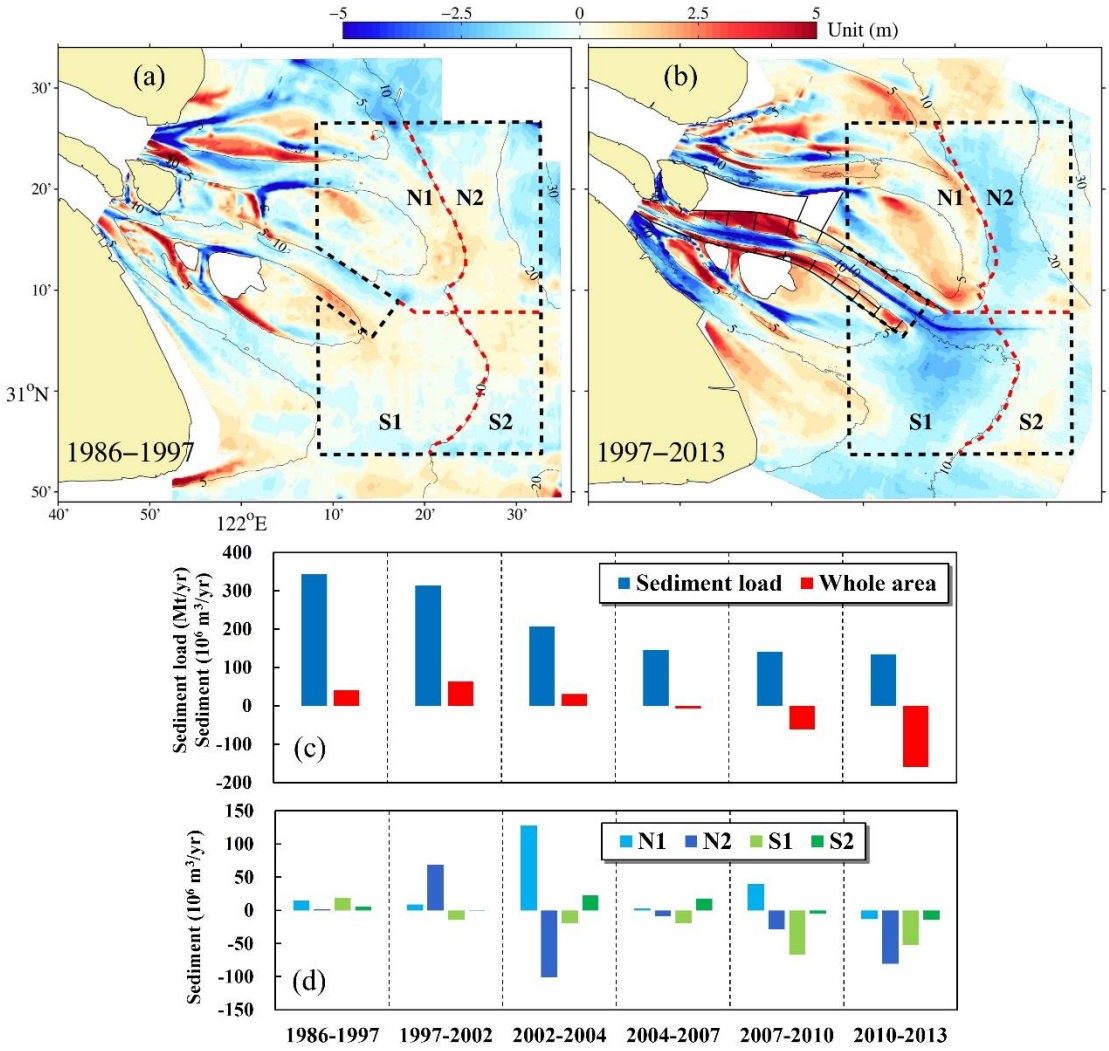

Fig. 4c; Tab. S2). The proportion of accretion area in the whole area decreased monotonously during the period 1986-2013 (Tab. S2), and the accretion area became less than

the erosion area after 2004 which was consistent with the trend of sediment volume changes.

Four sub-areas feature distinct morphological behaviors compared with the whole area in terms of sediment volume variations (

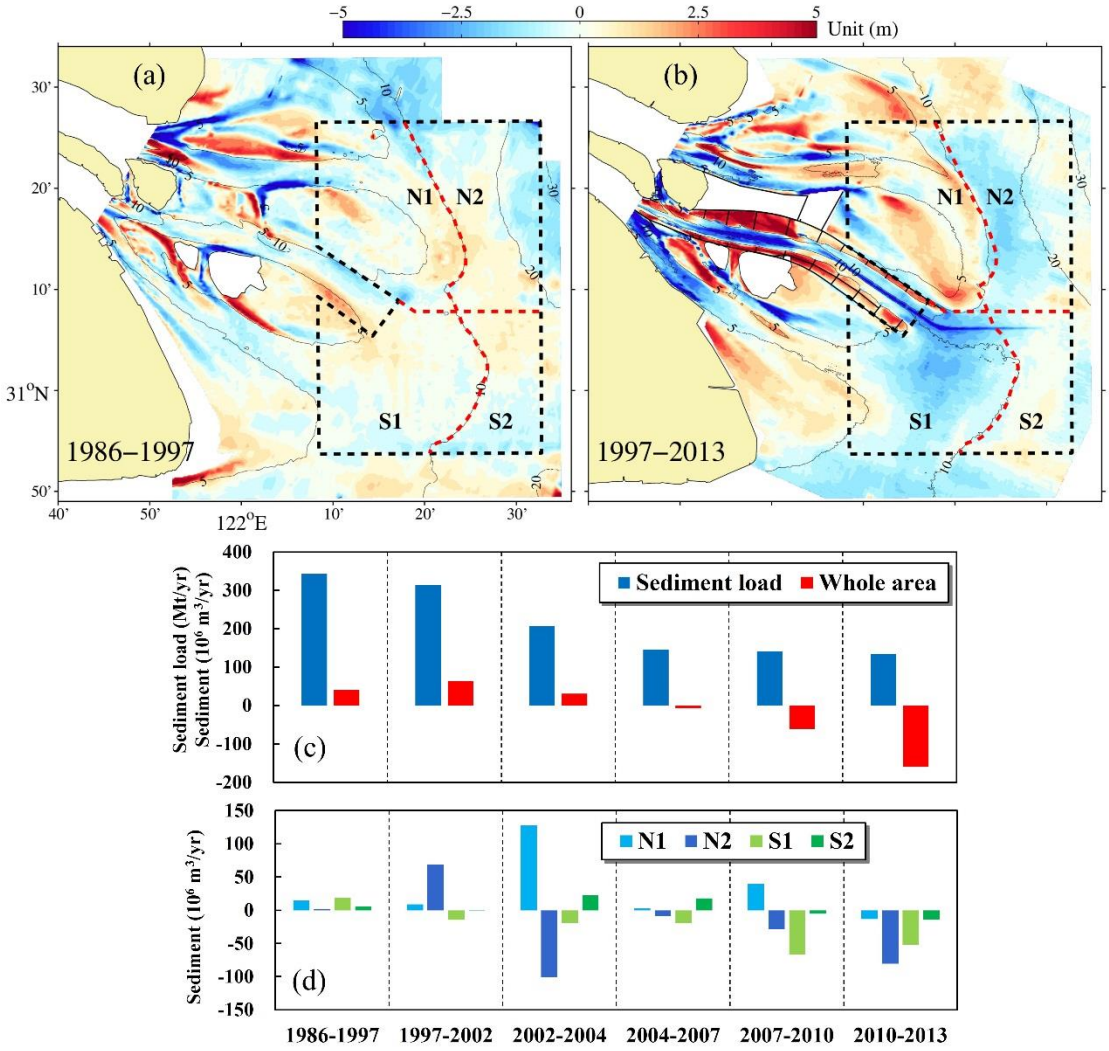

Fig. 4d). All the sub-areas were under net accretion in 1986-1997 with relatively low net accretion amount which was subject to bed sediment compaction. In the five periods from 1997 to 2013, the sub-areas involved alternate net accretion or erosion as described below. The Area N1, mainly covering the EHS, experienced net accretion in the first four periods and net erosion in the latest one. The net accretion volume and rate peaked in 2002-2004 (127.7

283 $Mm^3\ yr^{-1}$ or 195.2 mm yr^{-1}) (Tab. S3), and the values in other periods were relatively low.
284 This was also indicated by hypsometry curves of the northern part in which the shallow water
285 area (2~6.5 m) decreased abruptly from 2002 to 2004, suggesting rapid accretion (Fig. S2a).
286 The Area N2, representing the northern erosion zone, involved high accretion amount in
287 1997-2002 (68.6 $Mm^3\ yr^{-1}$) and altered into continuous erosion in the following four periods.
288 The strongest erosion was observed in 2002-2004 (−100.7 $Mm^3\ yr^{-1}$) corresponding to the
289 accretion peak of the Area N1. Afterwards, the net erosion amount dropped sharply to a low
290 value in 2004-2007 (−8.6 $Mm^3\ yr^{-1}$) and increased gradually to −80.6 $Mm^3\ yr^{-1}$ in 2010-2013.
291 Accordingly, the area deeper than 10 m increased remarkably twice, i.e. from 2002 to 2004
292 and from 2010 to 2013 (Fig. S2a). The Area S1, representing the southern erosion zone,
293 underwent increasing erosion in all the five periods except slightly decreased erosion rate in
294 2010-2013. Erosion in the southern part primarily occurred in the depth range of 5-10 m
295 which corresponded to the Area S1 (Fig. S2b). The total net erosion volume of the Area N2
296 was −50.5 $Mm^3\ yr^{-1}$ from 2002 to 2013, while the value of the Area S1 was −32.7 $Mm^3\ yr^{-1}$
297 from 1997 to 2013. The Area S2, representing adjacent part of the subaqueous delta,
298 converted from net accretion to net erosion around the year 2007. Both the accretion and
299 erosion amount were small suggesting slow morphological changes in this area. Notably, all
300 the sub-areas showed net erosion in 2010-2013, indicating that the mouth bar area had
301 undergone overall erosion under a low level of river sediment supply for a sufficiently long
302 time.

303 Variations of the typical cross-sections provide information on the erosion/deposition
304 thickness (Fig. 5). An erosion band along the north dike formed with deepening of 2 m in

1997-2013 (Fig. 5a, d). Both the accretion thickness at the central EHS and the erosion thickness at the northern erosion zone were nearly 2 m (Fig. 5a, d). The seabed at southeast end of the EHS had risen up to about 3.5 m in 1997-2013 (Fig. 5c, d). Meanwhile, the maximum erosion thickness of the southern erosion zone was about 2.5 m (Fig. 5b, d). The dredging activities caused continuous deepening of the navigation channel for more than 5 m (Fig. 5c).

4.2 Modeling the impacts of the DNCP on hydrodynamics and sediment transport

The flow and sediment transport fields with and without the training walls obtained by process-based simulations show characteristic differences (Fig. 6). The significant changes after the DNCP are identified within the North Passage, where the flow pattern is changed from rotating to reciprocating as indicated by the modeled feathers of tidal currents (Fig. 6a, c). This is also found by a previous modeling study (Hu and Ding, 2009). The flow features indicate that the flow pattern at the EHS is also changed from rotating to reciprocating with decreased flow velocity after the DNCP (Fig. 6a, c). This implies that the training walls induce weaker tidal current and longer tidal slack period. Besides, the tidal currents at the seaward end of the South and North Passage, corresponding to the erosion zone, are enhanced by the training walls, while the flow pattern remains almost unchanged (Fig. 6a, c). Bed-level changes in estuarine area are determined by the gradient of the residual sediment transport. The modeled monthly-averaged sediment flux without the training walls indicates positive gradient of residual sediment transport from the ESH to the North Channel suggesting erosion at the ESH (Fig. 6b). By contrast, negative gradient from the North Passage to the EHS with the training wall implies accretion at the later area (Fig. 6d). The gradient of residual sediment

transport at the seaward end of the North and South Passage is enhanced resulting from the presence of the training walls. The eroded sediment from the northern and southern erosion zone is converged by a sediment transport circulation system and transported into the North Passage with a much higher amount due to the training walls (Fig. 6b, d).

The differences of bed shear stress between numerical model runs are presented since sediment deposition or erosion processes are largely influenced by the bed shear stress (

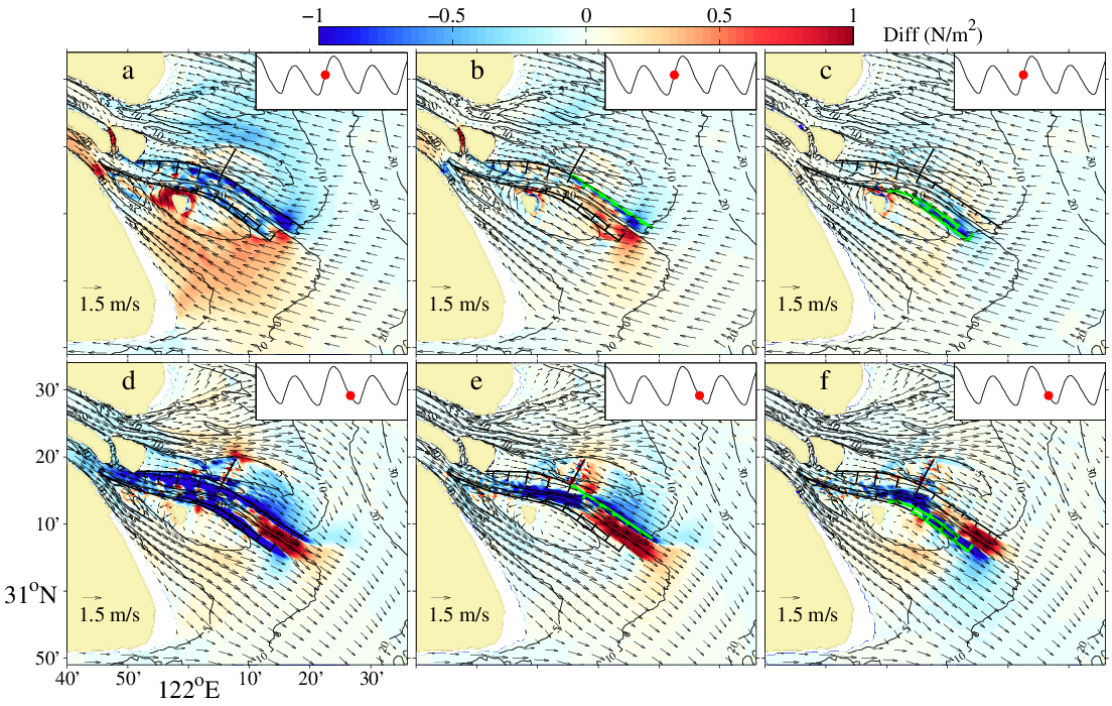

Fig. 7). The training walls cause decrease of the bed shear stress at the EHS at both flood and ebb maximum, while the bed shear stress at the seaward end of the North and South Passage is significantly enhanced only during rising tides (

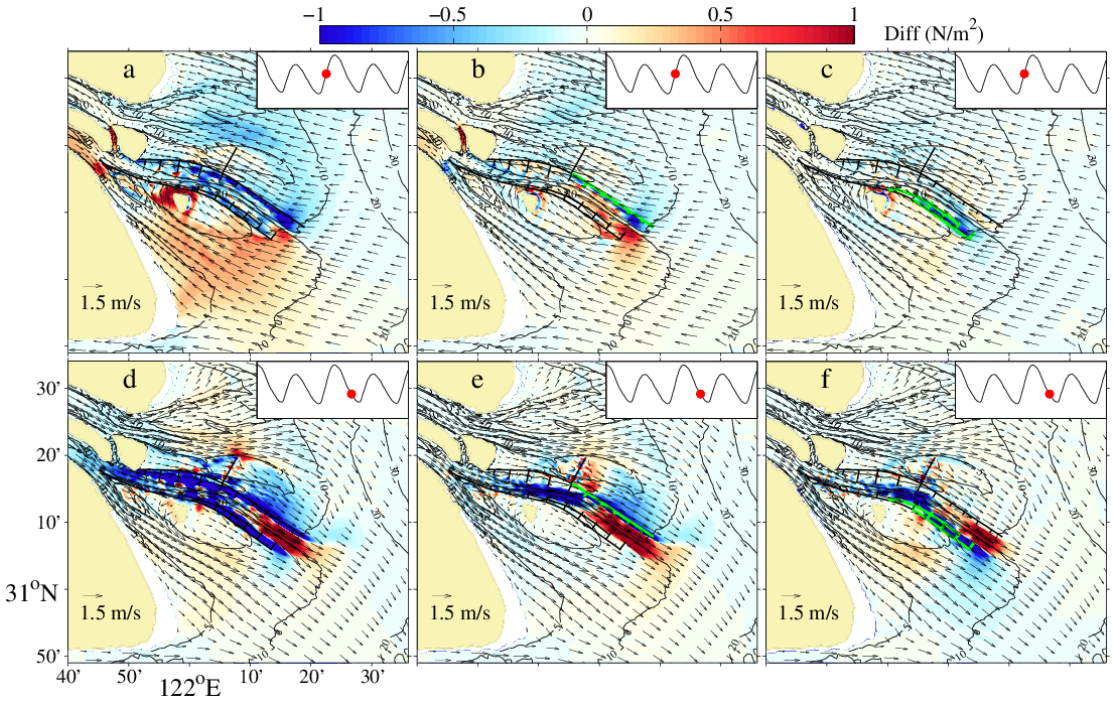

Fig. 7a, d). Modeling the impacts of the north dike shows similar results including the decrease at the EHS and increase at the southern erosion zone (

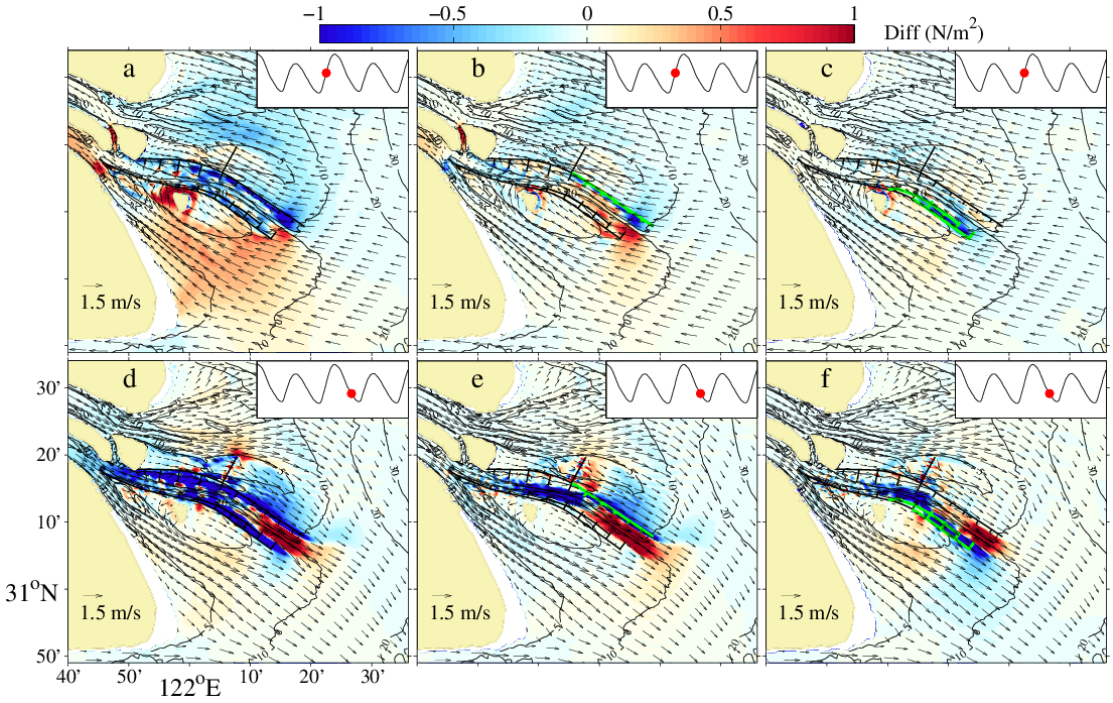

Fig. 7b, e). Moreover, the south dike results in limited impacts on the EHS and slightly

decrease of the bed shear stress in the southern area (

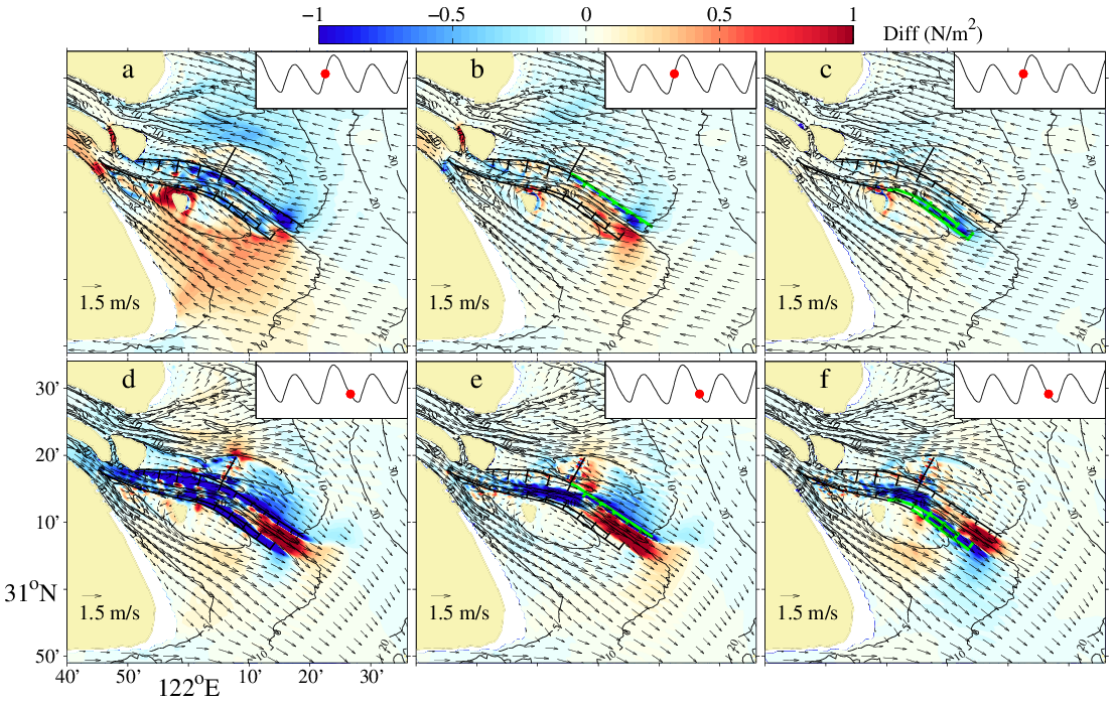

Fig. 7c, f).

4.3 Modeling the impacts of the DNCP on morphological changes

The modeled morphological changes under different configurations of the dikes and groynes provide direct evidence for the morphological impacts of the DNCPs (Fig. 8). The modeled and observed bed-level changes of the mouth bar area show qualitative agreement as described by Luan et al. (2017). Specifically, the accretion at the EHS and the erosion zones at the subaqueous delta are reproduced (Fig. 8a, b), which certifies the hindcast modeling as a reference case for investigating the observed evolution patterns at these areas. The difference between model runs with and without the training walls (Fig. 8c) is remarkable within the North Passage, including strong accretion within the dike-sheltered areas and erosion along the main channel due to the enhanced ebb flow. Excessive erosion at the entrance of the South

359 Passage is presented as the tidal currents are increased by the channel width narrowing and
360 the increase of flow diversion ratio. Notably, the model run with training walls produces more
361 accretion at the EHS which is identical with the location of the observed accretion zone at the
362 EHS. Moreover, erosion at the seaward end of the North and South Passage is enhanced after
363 including the training walls in the model. This area is consistent with the southern erosion
364 zone of the subaqueous delta. Similar results are obtained in numerical experiment on the
365 eastern half of the north dike, i.e. enhanced accretion at the EHS and erosion at the seaward
366 end of the North and South Passage (Fig. 8d). However, the patterns at these two areas are
367 absent in the results of the numerical experiment on the eastern half of the south dike which
368 only produces slight accretion at the southern erosion zone (Fig. 8e). It is suggested that the
369 impact of the south dike is limited relative to the north dike.
370
371 **5. Discussion**
372 5.1 Conversion from accretion to erosion due to river sediment reduction
373 The seaward part of the mouth bar area, which is defined as the study area for
374 quantifying morphological changes, has converted from accretion to overall erosion during
375 the period 1997-2013. This is consistent with the decreasing trend of the river sediment
376 discharge (Fig. 2) and a previous study by Yang et al. (2011). The mean sediment discharge
377 in the first decade after the TGD is less than 30% of the value in 1950s-1960s (Yang et al.,
378 2015). River sediment reduction results in decrease of the suspended sediment concentration
379 (SSC) in the estuarine area (Li et al., 2012; Liu et al., 2014). Based on statistical analysis of
380 measurements, Li et al. (2012) concluded that the mean surface SSC over the past 10-20 years

has decreased by 20-30% in the mouth bar area, which is lower than the 55% decrease in the inner estuary. The period coincides with the morphological evolution analysed in this study. Luan et al. (2016) suggested that the inner estuary has altered from deposition to erosion since 1980s, while present study indicates that the alteration in the seaward part of the mouth bar area occurs in the recent decade (

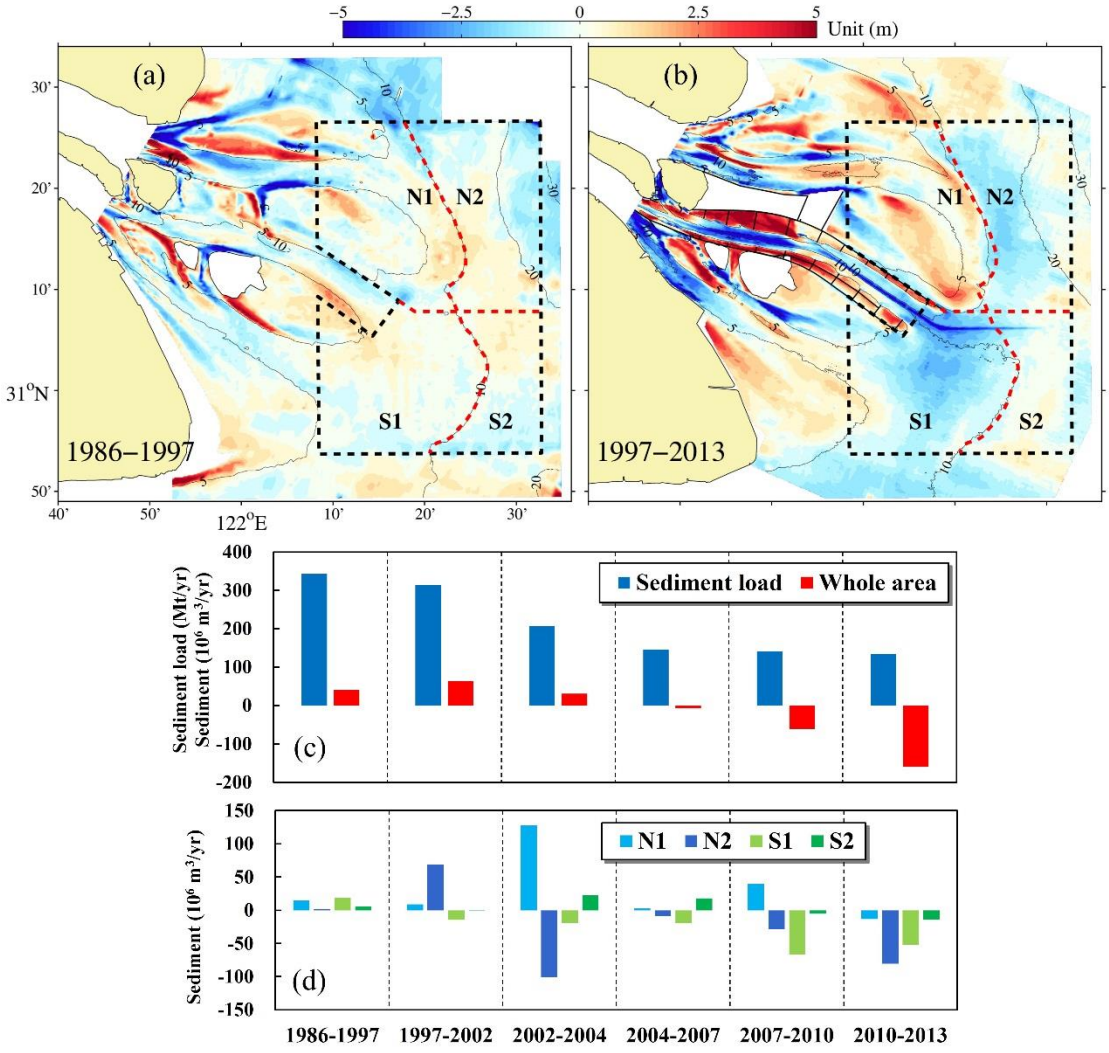

Fig. 4c).

The Yangtze subaqueous delta behaves as a depocenter which is estimated to accumulate more than 40% of the fluvial sediment in the past millennia (Milliman et al., 1985; Liu et al.,

2007), resulting in nearly 50 m of modern sediment at the mouth (Stanley and Chen, 1993). Therefore, the accretion rate of the mouth bar area deceased first as the sediment load started to decline in the 1980s, and the SSC within this area probably showed no apparent change. With the continuous river sediment decline, abundant bed sediment turned to compensate the decreasing SSC by erosion. Once the sediment load dropped below a critical level (Yang et al., 2003), the SSC in the mouth bar area started to decline which in turn intensified the erosion. This may explain that overall erosion of the whole study area occurred in 2010-2013 as the river sediment discharge remained a low value (Fig. 3e2; Fig. 4d). Li et al. (2012) also reported that the mean surface SSC in the north of the

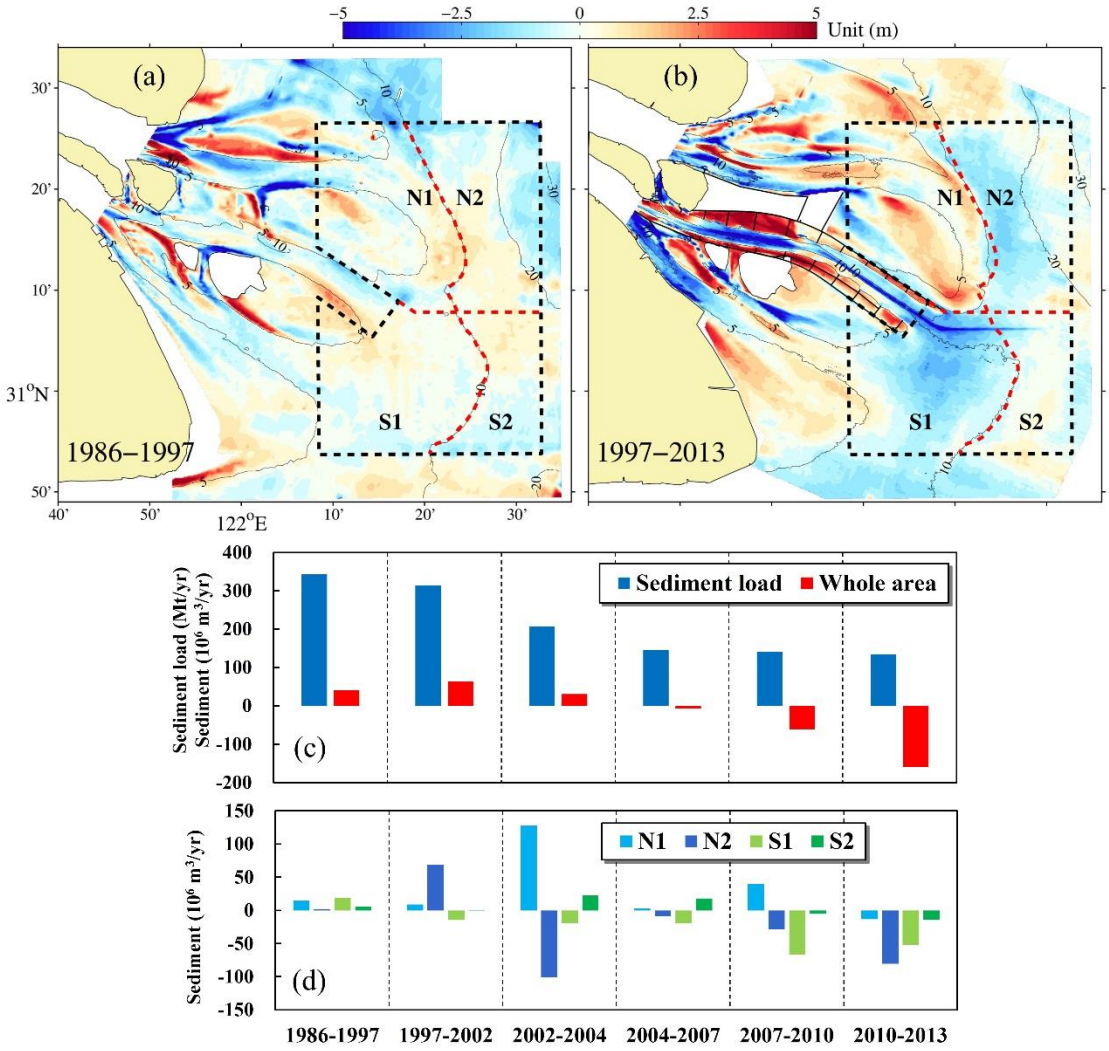

mouth bar area showed much lower decrease rate (e.g., 5% at Sheshan Station) than the south (e.g., 30% at Dajishan Station). This suggests that more bed sediment in the north is resuspended to partly offset the SSC decrease, and may explain more erosion in the Area N2 than the Area S1 (

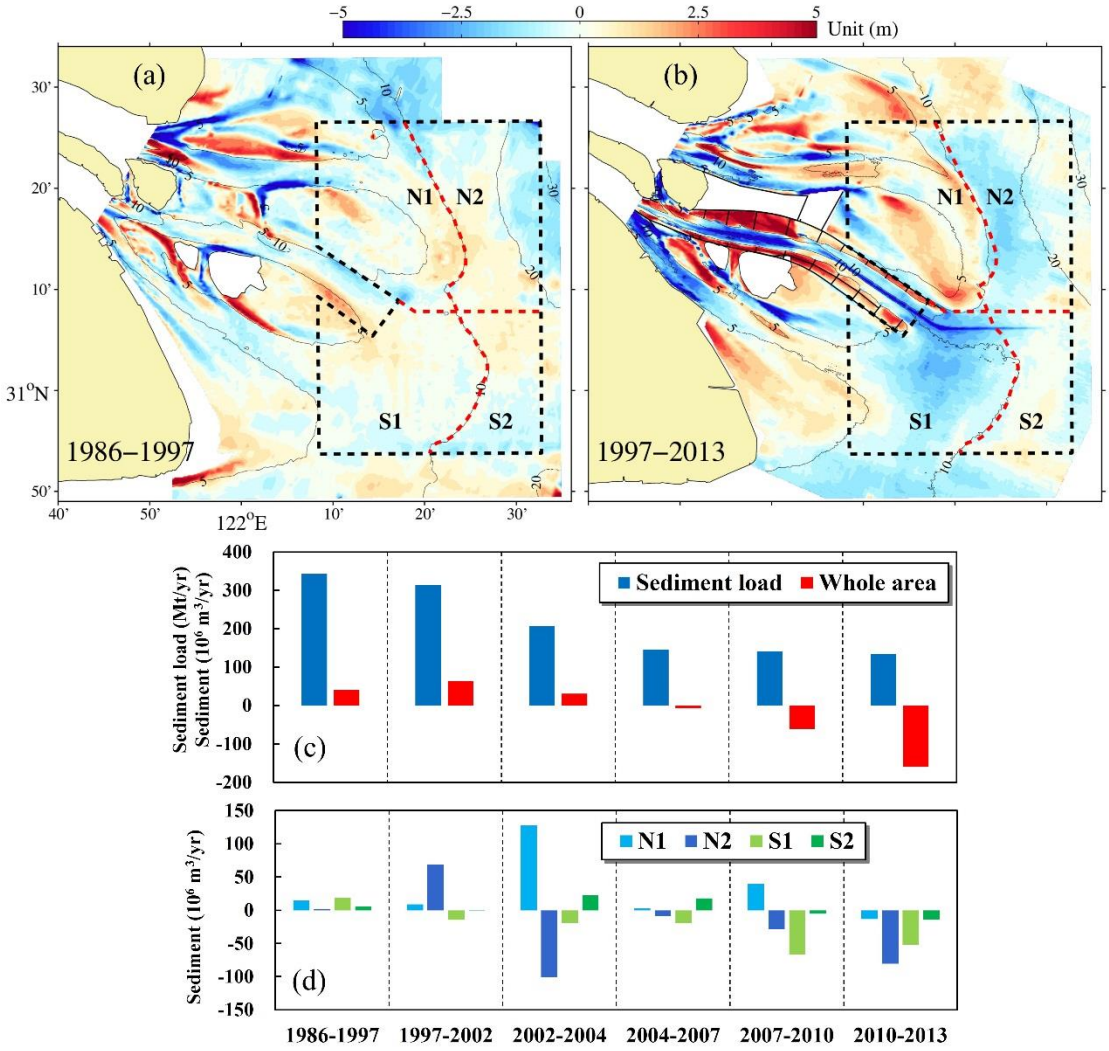

Fig. 4d).

Generally, delta progradation or regression depends on the sediment budget between fluvial supply and offshore dispersal (Syvitski and Saito, 2007; Canestrelli et al., 2010). Under decreasing river sediment supply and relatively stable dispersal amount by coastal

411 currents (Deng et al., 2017), the erosion of Yangtze subaqueous delta seems to be an
412 inevitable tendency. Since the navigation channel and the North Passage between the twin
413 dikes are excluded from the study area, the morphological changes of the open coastal waters
414 as concerned show limited immediate impacts by training walls (e.g., rapid deposition in the
415 dike-sheltered areas). Therefore, the decreasing river sediment supply is identified as the
416 prime cause for the accretion-erosion conversion of the seaward part of the mouth bar area.

417 5.2 Distinct morphodynamic features due to the training walls

418 With the overall evolution pattern, morphodynamics of the Yangtze mouth bar area show
419 distinct spatiotemporal variations during 1997-2013. One remarkable feature is the enhanced
420 accretion at the EHS
421 (

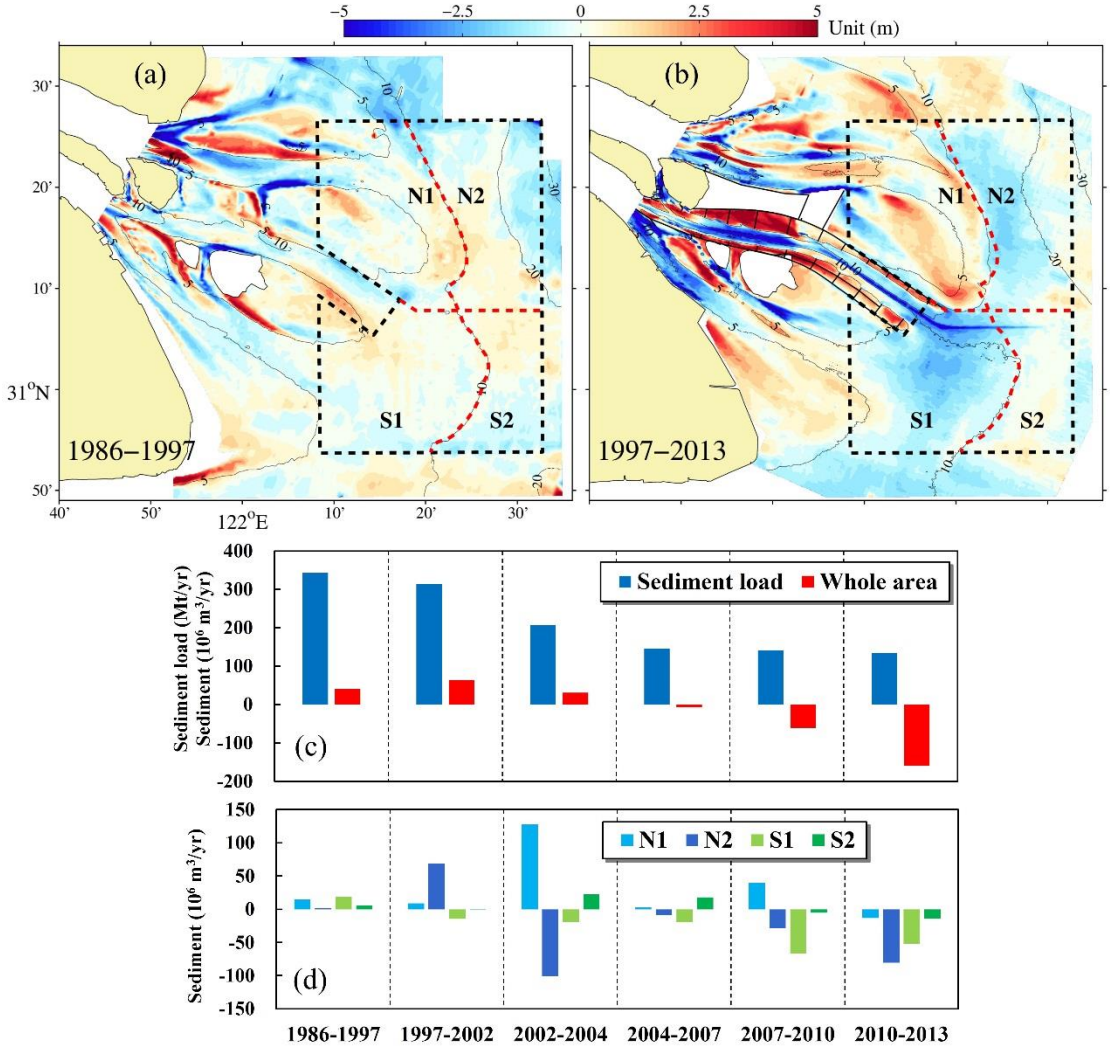

422

423 Fig. 4b), which is inconsistent with the evolution trend of the whole study area. As

424 indicated by the hydrodynamic and morphological modeling results, the reciprocating flow

425 pattern with weaker tidal current and longer slack period at the EHS after the construction of

426 dikes implies a depositional environment. This is verified by the observed continuous

427 accretion of the EHS in 1997-2010. Particularly, the peak of the accretion amount occurred in

428 2002-2004 during which the dikes were extended to the present location in Phase II (Fig. 1c).

429 Though the SSC around the mouth bar area showed decreasing trend, the suspended sediment

430 transported by the flood currents was easier to settle and accumulate at the EHS. Thus, the

431 EHS converted to a sediment-starved status after the DNCP. Moreover, the accretion peak of

the EHS occurred simultaneously with the erosion peak of the northern erosion zone (

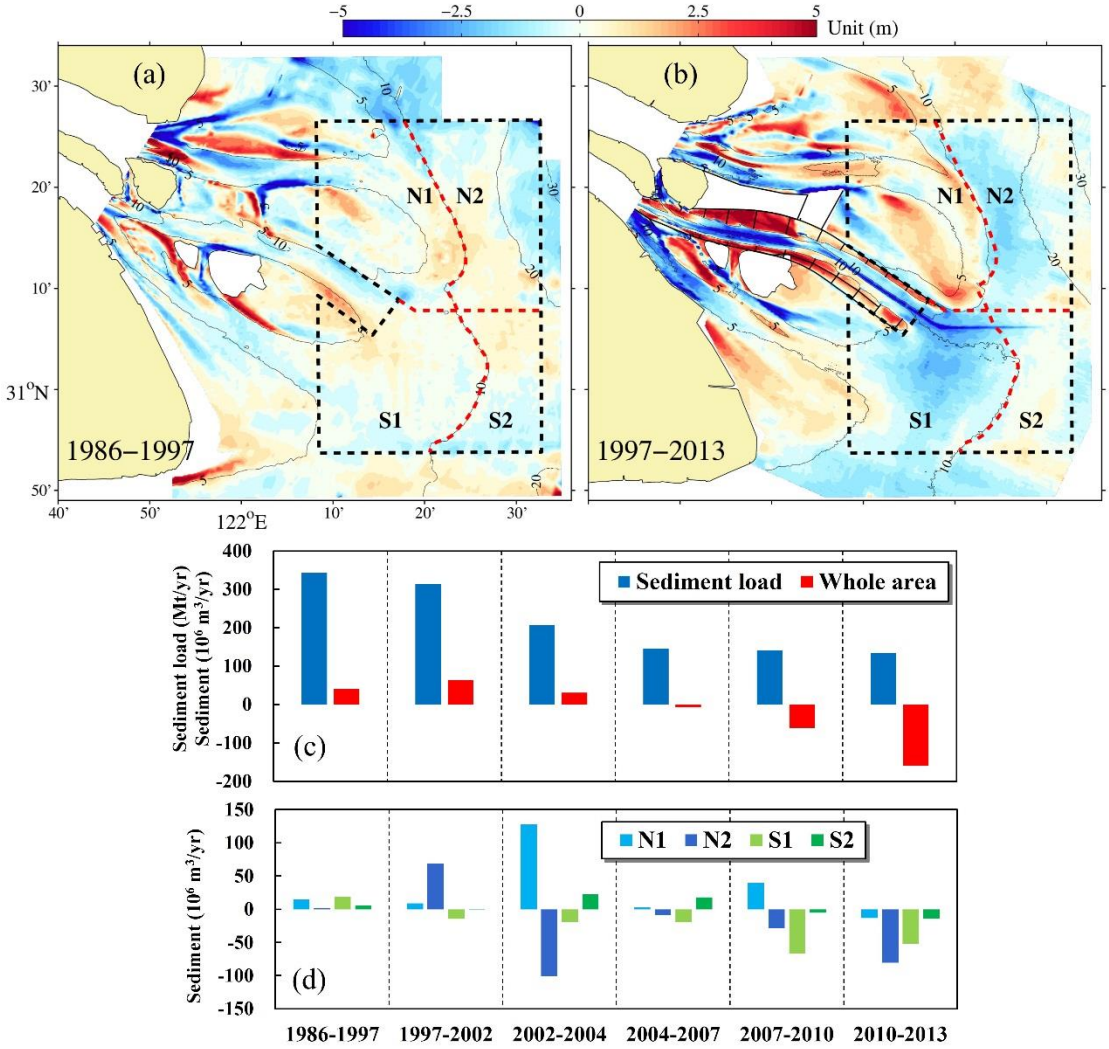

Fig. 4d). The modeled sediment flux indicates that the eroded sediment at the subaqueous delta could be the important source for the accretion at the EHS under decreasing SSC. In sum, the enhanced accretion at the EHS was caused by the training walls along the North Passage, particularly the north dike, which changed the hydrodynamics and sediment transport patterns around the EHS.

Another evolution feature is the formation of the erosion zones at the subaqueous delta (

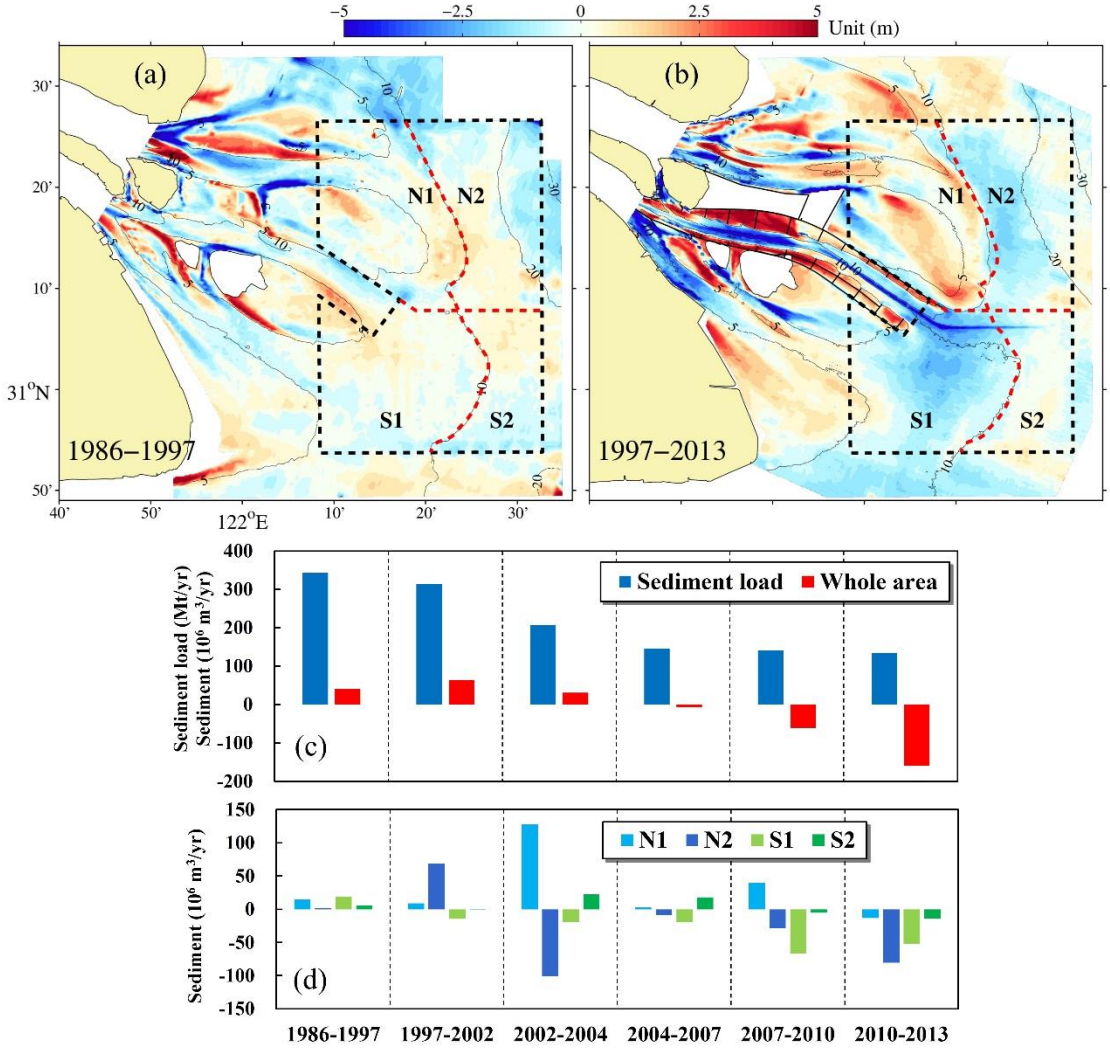

Fig. 4b). Though the Yangtze delta erosion is controlled by the river sediment reduction as discussed previously, it can be influenced by large-scale estuarine engineering projects. Model results demonstrate that the training walls enhance the hydrodynamic condition at the southern erosion zone during flood tide, and that the enhancement is mainly attributed to the presence of the north dike (Fig. 7). Subsequently, the modeled bed level changes show stronger erosion at the southern erosion zone due to the training walls (Fig. 8c, d). It is notable that the erosion zones at the subaqueous delta are the estuarine muddy areas where the seabed is mainly composed of unconsolidated fine-grained sediment (Fig. S3). These muddy areas are subject to intensive sediment exchange between the water column and seabed

452 through sediment deposition and resuspension (Liu et al., 2010). Therefore, bed level changes
453 of these areas are more sensitive to variations of the SSC and hydrodynamic condition than
454 other areas covered by coarser sediment. The muddy areas are likely to involve the earliest
455 erosion in the subaqueous delta in response to the decreasing river sediment supply, and the
456 erosion is accelerated after the construction of the training walls, especially the north dike.
457 Based on the morphological evolution analysis and numerical simulations above, the
458 sediment transport paths and specific erosion/deposition locations within the study area before
459 and after the DNCP are schematized as shown in Fig. 9. Before the DNCP in 1997, the north
460 part of the mouth bar area was under accretion with higher accretion rate at the mouth of the
461 North Channel than the EHS, while erosion has occurred at the seaward end of the North and
462 South Passage (Fig. 9a). The eroded sediment was involved in a circulation system and was
463 partly delivered to the outer sea by tidal currents. After the DNCP, suspended sediment driven
464 by tidal currents tended to deposit at the EHS after the north dike was extended to its present
465 location. Thereby, accretion at the EHS was largely enhanced (Fig. 9b). Meanwhile, the
466 mouth of the North Channel converted from accretion to strong erosion, which is regarded as
467 the northern erosion zone within the study area
468 (

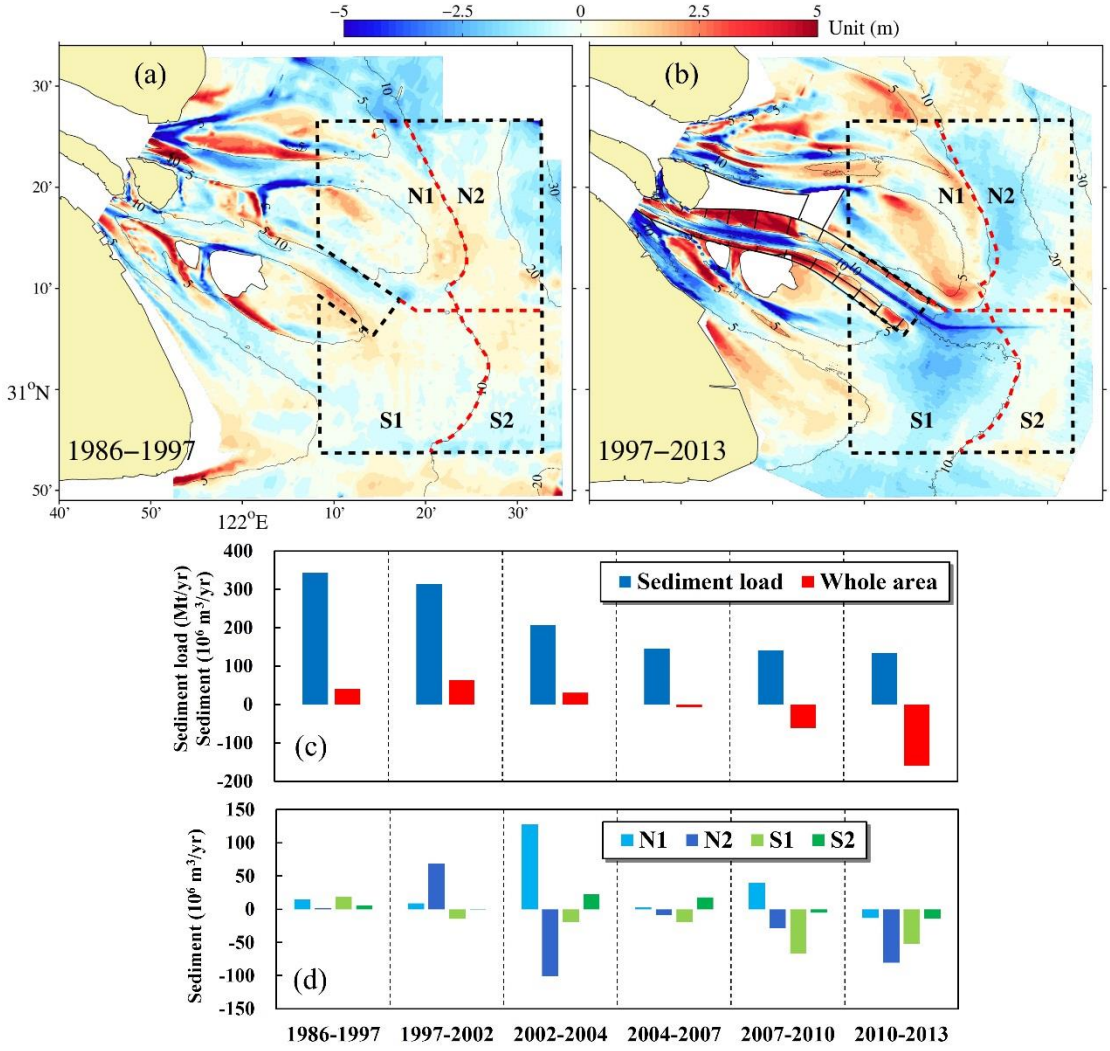

469

470 Fig. 4b). Erosion at the seaward end of the North and South Passage was enhanced by
471 the training walls superimposed upon the river sediment reduction. Part of the eroded
472 sediment from both erosion zones was combined and transported away to the outer sea, while
473 the rest passed across the south dike and may become a considerable source for back-siltation
474 of the navigation channel along the North Passage (Zhu et al., 2016).

475 5.3 Implications for deltaic morphodynamic equilibrium and sustainability

476 A widely concerned issue for deltaic morphodynamics is the equilibrium morphological
477 configurations and the timescale to approach them in response to natural forcing changes and
478 human interventions (Zhou et al., 2017). Under sufficient sediment supply, the

morphodynamic equilibrium of a propagating river delta usually refers to its growth limit. Gao (2007) suggested that the growth limit of the Yangtze delta is constrained by multiple factors, including the original bathymetry, sediment supply and retention, sea-level rise and bed subsidence. Conceptual geometric models proposed by Gao (2007) indicates that the Yangtze Delta will reach its growth limit in the near future under river sediment reduction. Controlled by the variation of sediment discharge, the Yangtze subaqueous delta experienced rapid accretion in 1950s-1960s, decreased accretion since 1980s and regional erosion in the recent decade (Yang et al., 2011; Dai et al., 2014; Luan et al., 2016). Though the sediment load remained relatively stable at a low level (~140 Mt yr^{-1}) after 2004 (Fig. 2), the net erosion amount of the study area increased almost linearly (

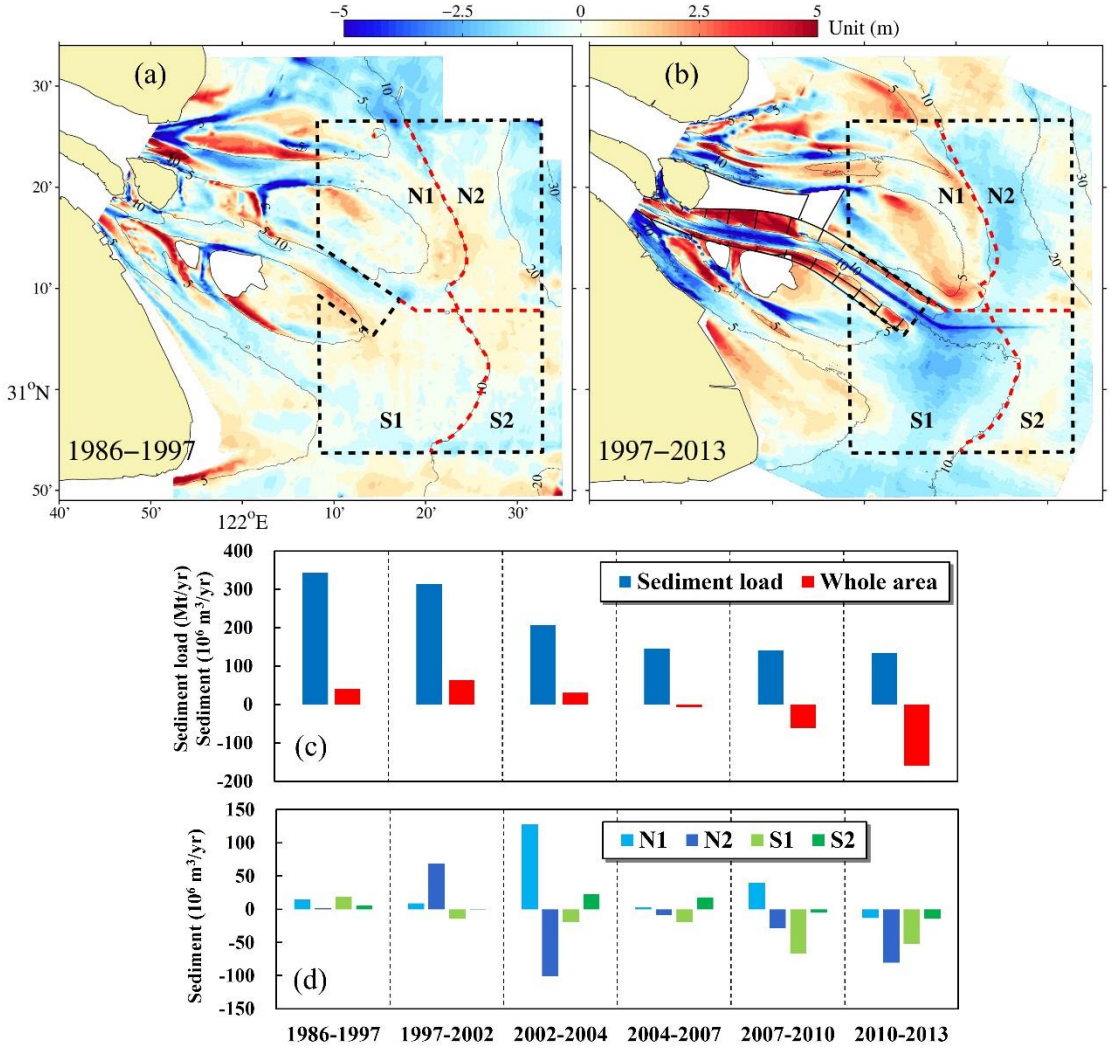

Fig. 4c) until the 2010-2013 when all the four sub-areas were under net erosion in 2010-2013, which is just the opposite of net accretion of four sub-areas in 1986-1997. On the one hand, this is probably because the sediment discharge had already dropped below a critical value for converting from accretion to erosion, and the fine-grained sediment within the muddy areas was continuously eroded to compensate the decreasing SSC. This also explains the time lag between the decrease in SSC within the estuarine waters and the decrease in sediment discharge (Li et al., 2012). On the other hand, the training walls along the North Passage enhanced the erosion at the southern erosion zone (Fig. 8c). Thus it can be concluded that the Yangtze subaqueous delta is accelerating to approach the morphodynamic

500 equilibrium due to the impacts of large-scale estuarine engineering projects.

501 Considering that the observed erosion zones contain abundant fine-grained sediment, the
502 present erosion thickness has not yet reached the maximum, and deepening is likely to
503 continue in the future until the dynamic equilibrium. The erosion limit and timescale for
504 approaching to the equilibrium is determined by balance between the decreasing erosional
505 ability of tidal currents due to continuous deepening and increasing anti-erosional ability of
506 the seabed due to armoring and increased compaction of deeper sediment. According to the
507 variation of hypsometry curves, the sub-area N2 converted from accretion to erosion around
508 the year 2002. The area deeper than 20 m within the N2 in 2013 returned to nearly the same
509 value in 1997, while the area shallower than 20 m in 2013 has already showed net erosion
510 relative to the year 1997. It is suggested that deeper area is less sensitive to the conversion
511 from accretion to erosion, and that the deeper subaqueous delta may reach the equilibrium in
512 an earlier stage.

513 Similar situations can also be found in other estuarine and coastal areas around the world.
514 Generally, the timescale for estuaries and deltas towards a new morphodynamic equilibrium
515 after human interventions is determined by hydrodynamic condition (e.g., tide, wave, and
516 river flow), sediment supply and property, and geological and landform setting of the systems.
517 The Mersey Estuary, a tidal dominant estuary on the west coast of the UK, experienced
518 significant accretion in 1906-1977 due to the construction of training walls and dredging
519 activity, and evolved towards an equilibrium estuary state over a period of approximately 70
520 years (Thomas et al., 2002). The construction of a large-scale closure dam (Afsluitdijk) in the
521 Dutch Wadden Sea in 1932 has disturbed the equilibrium condition of adjacent tidal basins,

522 which are still adapting to the human intervention after nearly 80 years and on the way to a
523 new dynamic equilibrium state (Elias et al., 2003; Dastgheib et al., 2008). The Eastern
524 Scheldt estuary showed overall erosion at the ebb-tidal delta and tidal flats within the estuary
525 after the construction of the storm surge barrier in 1986 (Eelkema et al., 2013; Wang et al.,
526 2015; de Vet et al., 2017), and the estuary is far from any kind of equilibrium at present
527 (Eelkema et al., 2013). The responding time of the Yangtze subaqueous delta to large-scale
528 estuarine engineering projects remains unknown and merits further systematic research.

529 Among the global dataset of deltas, the Yangtze delta is a typical example under
530 interactive impacts of river input changes and human activities (Syvitski et al., 2009; Tessler
531 et al., 2015). Day et al. (1997, 2016) considered delta sustainability from geomorphic,
532 ecological, and economic perspectives. The geomorphic functioning and sustainability of the
533 Yangtze subaqueous delta can be affected by large-scale estuarine engineering projects. For
534 instance, the continuous erosion at the subaqueous delta may cause engineering failure and
535 increase the exposure risk of buried oil/gas pipelines. Another example is the EHS which is
536 proposed to build an excavated harbor basin to meet the increasing shipping demand (Ding
537 and Li, 2013). Though the dike-induced accretion at the EHS is favorable for the harbor
538 construction, net erosion was observed at the EHS after 2010. Therefore, Yangtze delta
539 sustainability calls for continuous bathymetry observation and reliable prediction on future
540 evolution trend of the mouth bar area under continuous decrease in sediment discharge as
541 predicted (Yang et al., 2014).

542

543 **6. Conclusions**

544 This study addresses the morphodynamic evolution processes of the mouth bar area of
545 the Yangtze Estuary in 1997-2013 using observed bathymetric data. The results reveal that the
546 seaward part of the mouth bar area, defined as the study area for calculation of sediment
547 volume change, converted from net accretion to net erosion around the year 2004. The prime
548 cause for this conversion is the river sediment reduction, which induced the decrease in SSC
549 around the mouth bar area and thereby sediment compensation of the subaqueous delta by
550 erosion. Though the sediment discharge remained relatively stable at a low level (~140 Mt
551 yr^{-1}) after 2004, the erosion rate of the study area increased almost linearly, suggesting that
552 the erosion were accelerating. The erosion/deposition patterns of the study area show distinct
553 spatial variations during the period 1997-2013. Specifically, an erosion zone formed at the
554 mouth of the North Channel after 2002 with the erosion rate peak in 2002-2004 and the
555 overall erosion thickness nearly 2 m. Another erosion zone formed at the seaward end of the
556 North and South Passage after 1997 with increasing erosion rate and larger overall erosion
557 thickness than the northern one. The erosion volumes of both the northern and southern
558 erosion zones increased gradually after 2004. Meanwhile, the EHS involved abnormal
559 accretion under the trend of decreasing sediment discharge, especially the strongest accretion
560 in 2002-2004. The net accretion status of the EHS was retained until 2010.

561 Process-based modeling approach (Delft3D) is applied to investigate the morphological
562 impacts of large-scale estuarine engineering projects on the mouth bar area, considering that
563 the study period of morphological evolution coincides with the construction period of the
564 DNCP along the North Passage (1997-2010). Hydrodynamic simulations indicate that the
565 training walls change the flow pattern at the EHS from rotating flows to reciprocating flows

566 with decreased flow velocity, particularly decrease the bed shear stress at the EHS during ebb
567 tide. Longer tidal slack period and weaker hydrodynamic condition characterize the EHS as a
568 depositional environment, which is consistent with the modeled sediment flux. The flow
569 pattern at the southern erosion zone shows no evident change after the DNCP, whereas the
570 tidal flows are enhanced as reflected by larger bed shear stress during flood tide.
571 Morphological modeling results show that the training walls enhanced the accretion at the
572 EHS and erosion at the southern erosion zone, and these impacts are primarily contributed by
573 the north dike. This can also verified by the extension of the twin dikes to the present
574 locations in Phase II (2002-2004) and simultaneous accretion peak of the EHS. The Yangtze
575 subaqueous delta is accelerating towards the morphodynamic equilibrium under large-scale
576 estuarine engineering projects superimposed with river sediment reduction. The timescale for
577 approaching to the erosion limit remained unknown, and calls for further systematic research
578 to support the sustainable management of this large-scale estuarine system.
579
580 **Acknowledgments**
581 This study is financed by…
582
583 **References**
584 Anthony, E.J., Brunier, G., Besset, M., Goichot, M., Dussouillez, P., Nguyen, V.L., 2015.
585 Linking rapid erosion of the Mekong River delta to human activities. Sci. Rep.-UK 5,
586 14745.
587 Blott, S.J., Pye, K., van der Wal, D., Neal, A., 2006. Long-term morphological change and its

588 causes in the Mersey Estuary, NW England. Geomorphology 81, 185-206.
589 Blum, M.D., Roberts, H.H., 2009. Drowning of the Mississippi Delta due to insufficient
590 sediment supply and global sea-level rise. Nat. Geosci. 2, 488-491.
591 Canestrelli, A., Fagherazzi, S., Defina, A., Lanzoni, S., 2010. Tidal hydrodynamics and
592 erosional power in the Fly River delta, Papua New Guinea. Journal of Geophysical
593 Research: Earth Surface 115, F4033.
594 Chen, J., Zhu, H., Dong, Y., Sun, J., 1985. Development of the Changjiang estuary and its
595 submerged delta. Cont. Shelf Res. 4, 47-56.
596 Chu, Z.X., Sun, X.G., Zhai, S.K., Xu, K.H., 2006. Changing pattern of accretion/erosion of
597 the modern Yellow River (Huanghe) subaerial delta, China: Based on remote sensing
598 images. Mar. Geol. 227, 13-30.
599 Coleman, J.M., Wright, L.D., 1975. Modern river deltas: variability of processes and sand
600 bodies,in: Broussard, M.L. (Ed.), Deltas: Models for Exploration. Houston Geological
601 Society, pp. 99-149.
602 Dai, Z., Liu, J.T., Fu, G., Xie, H., 2013. A thirteen-year record of bathymetric changes in the
603 North Passage, Changjiang (Yangtze) estuary. Geomorphology 187, 101-107.
604 Dai, Z., Liu, J.T., Wei, W., Chen, J., 2014. Detection of the Three Gorges Dam influence on
605 the Changjiang (Yangtze River) submerged delta. Sci. Rep.-UK 4, 6600.
606 Dastgheib, A., Roelvink, J.A., Wang, Z.B., 2008. Long-term process-based morphological
607 modeling of the Marsdiep Tidal Basin. Mar. Geol. 256, 90-100.
608 Day, J., Hall, C.S., Kemp, W.M., Yanez-Aranciba, A., 1989. Estuarine Ecology. John-Wiley,
609 New York.

610 Day, J.W., Martin, J.F., Cardoch, L., Templet, P.H., 1997. System functioning as a basis for
611 sustainable management of deltaic ecosystems. Coast. Manage. 25, 115-153.
612 de Vet, P.L.M., van Prooijen, B.C., Wang, Z.B., 2017. The differences in morphological
613 development between the intertidal flats of the Eastern and Western Scheldt.
614 Geomorphology 281, 31-42.
615 De Vriend, H., Wang, Z., Ysebaert, T., Herman, P.J., Ding, P., 2011. Eco-Morphological
616 Problems in the Yangtze Estuary and the Western Scheldt. Wetlands 31, 1033-1042.
617 Deng, B., Wu, H., Yang, S., Zhang, J., 2017. Longshore suspended sediment transport and its
618 implications for submarine erosion off the Yangtze River Estuary. Estuarine, Coastal and
619 Shelf Science 190, 1-10.
620 Ding, P.X., Li, S.G., 2013. Planning ideas and key technology for building excavated-in
621 harbor basin in the Hengsha Shoal of the Yangtze Estuary. Journal of East China Normal
622 University (Natural Sciences), 1-9 (in Chinese with English abstract).
623 Dissanayake, D.M.P.K., Wurpts, A., Miani, M., Knaack, H., Niemeyer, H.D., Roelvink, J.A.,
624 2012. Modelling morphodynamic response of a tidal basin to an anthropogenic effect: Ley
625 Bay, East Frisian Wadden Sea – applying tidal forcing only and different sediment
626 fractions. Coast. Eng. 67, 14-28.
627 Eelkema, M., Wang, Z.B., Hibma, A., Stive, M.J., 2013. Morphological effects of the Eastern
628 Scheldt storm surge barrier on the ebb-tidal delta. Coast. Eng. J. 55, 1350010.
629 Elias, E., Stive, M.J.F., Bonekamp, H., Cleveringa, J., 2003. Tidal inlet dynamics in response
630 to human intervention. Coast. Eng. J. 45, 629-658.
631 Ericson, J.P., Vörösmarty, C.J., Dingman, S.L., Ward, L.G., Meybeck, M., 2006. Effective

632 sea-level rise and deltas: Causes of change and human dimension implications. Global
633 Planet. Change 50, 63-82.
634 Gao, S., 2007. Modeling the growth limit of the Changjiang Delta. Geomorphology 85,
635 225-236.
636 Giosan, L., Syvitski, J., Constantinescu, S., Day, J., 2014. Climate change: protect the world's
637 deltas. Nature 516, 31-33.
638 Guo, L., van der Wegen, M., Roelvink, J.A., He, Q., 2014. The role of river flow and tidal
639 asymmetry on 1D estuarine morphodynamics. Journal of Geophysical Research: Earth
640 Surface 119.
641 Hori, K., Saito, Y., Zhao, Q., Cheng, X., Wang, P., Sato, Y., Li, C., 2001. Sedimentary facies
642 and Holocene progradation rates of the Changjiang (Yangtze) delta, China.
643 Geomorphology 41, 233-248.
644 Hu, K., Ding, P., 2009. The Effect of Deep Waterway Constructions on Hydrodynamics and
645 Salinities in Yangtze Estuary, China. J. Coastal Res., 961-965.
646 Lesser, G.R., Roelvink, J.A., van Kester, J.A.T.M., Stelling, G.S., 2004. Development and
647 validation of a three-dimensional morphological model. Coast. Eng. 51, 883-915.
648 Li, P., Yang, S.L., Milliman, J.D., Xu, K.H., Qin, W.H., Wu, C.S., Chen, Y.P., Shi, B.W.,
649 2012. Spatial, Temporal, and Human-Induced Variations in Suspended Sediment
650 Concentration in the Surface Waters of the Yangtze Estuary and Adjacent Coastal Areas.
651 Estuar. Coast. 35, 1316-1327.
652 Liu, G., Zhu, J., Wang, Y., Wu, H., Wu, J., 2011. Tripod measured residual currents and
653 sediment flux: Impacts on the silting of the Deepwater Navigation Channel in the

654 Changjiang Estuary. Estuarine, Coastal and Shelf Science 93, 192-201.
655 Liu, H., He, Q., Wang, Z., Weltje, G.J., Zhang, J., 2010. Dynamics and spatial variability of
656 near-bottom sediment exchange in the Yangtze Estuary, China. Estuarine, Coastal and
657 Shelf Science 86, 322-330.
658 Liu, J.H., Yang, S.L., Zhu, Q., Zhang, J., 2014. Controls on suspended sediment
659 concentration profiles in the shallow and turbid Yangtze Estuary. Cont. Shelf Res. 90,
660 96-108.
661 Liu, J.P., Xu, K.H., Li, A.C., Milliman, J.D., Velozzi, D.M., Xiao, S.B., Yang, Z.S., 2007.
662 Flux and fate of Yangtze River sediment delivered to the East China Sea. Geomorphology
663 85, 208-224.
664 Luan, H.L., Ding, P.X., Wang, Z.B., Ge, J.Z., 2017. Process-based morphodynamic modeling
665 of the Yangtze Estuary at a decadal timescale: Controls on estuarine evolution and future
666 trends. Geomorphology 290, 347-364.
667 Luan, H.L., Ding, P.X., Wang, Z.B., Ge, J.Z., Yang, S.L., 2016. Decadal morphological
668 evolution of the Yangtze Estuary in response to river input changes and estuarine
669 engineering projects. Geomorphology 265, 12-23.
670 Luo, X.X., Yang, S.L., Wang, R.S., Zhang, C.Y., Li, P., 2017. New evidence of Yangtze delta
671 recession after closing of the Three Gorges Dam. Sci. Rep.-UK 7.
672 Luo, X.X., Yang, S.L., Zhang, J., 2012. The impact of the Three Gorges Dam on the
673 downstream distribution and texture of sediments along the middle and lower Yangtze
674 River (Changjiang) and its estuary, and subsequent sediment dispersal in the East China
675 Sea. Geomorphology 179, 126-140.

676 Milliman, J.D., Farnsworth, K.L., 2013. River discharge to the coastal ocean: a global
677 synthesis. Cambridge University Press, Cambridge.
678 Milliman, J.D., Shen, H.T., Yang, Z.S., Mead, R.H., 1985. Transport and deposition of river
679 sediment in the Changjiang estuary and adjacent continental shelf. Cont. Shelf Res. 4,
680 37-45.
681 Milliman, J.D., Yun-Shan, Q., Mei-E, R., Saito, Y., 1987. Man's Influence on the Erosion and
682 Transport of Sediment by Asian Rivers: The Yellow River (Huanghe) Example. The
683 Journal of Geology 95, 751-762.
684 Morton, R.A., Bernier, J.C., Barras, J.A., Ferina, N.F., 2005. Rapid subsidence and historical
685 wetland loss in the Mississippi delta plain: likely causes and future implications, US Geol.
686 Surv., Washington, DC.
687 Renaud, F.G., Syvitski, J.P., Sebesvari, Z., Werners, S.E., Kremer, H., Kuenzer, C., Ramesh,
688 R., Jeuken, A., Friedrich, J., 2013. Tipping from the Holocene to the Anthropocene: How
689 threatened are major world deltas? Curr. Opin. Env. Sust. 5, 644-654.
690 Roelvink, J.A., 2006. Coastal morphodynamic evolution techniques. Coast. Eng. 53, 277-287.
691 Sanchez-Arcilla, A., Jimenez, J.A., Valdemoro, H.I., 1998. The Ebro Delta: Morphodynamics
692 and Vulnerability. J. Coastal Res. 14, 755-772.
693 Stanley, D.J., 1996. Nile delta: extreme case of sediment entrapment on a delta plain and
694 consequent coastal land loss. Mar. Geol. 129, 189-195.
695 Stanley, D.J., Chen, Z., 1993. Yangtze delta, eastern China: 1. Geometry and subsidence of
696 Holocene depocenter. Mar. Geol. 112, 1-11.
697 Stanley, D.J., Warne, A.G., 1994. Worldwide Initiation of Holocene Marine Deltas by

698 Deceleration of Sea-Level Rise. Science 265, 228-231.
699 Su, M., Yao, P., Wang, Z.B., Zhang, C.K., Stive, M.J.F., 2016. Exploratory morphodynamic
700 hindcast of the evolution of the abandoned Yellow River delta, 1578-1855 AD. Mar. Geol.
701 Syvitski, J.P.M., 2008. Deltas at risk. Sustain. Sci. 3, 23-32.
702 Syvitski, J.P.M., Kettner, A., 2011. Sediment flux and the Anthropocene. Phil. Trans. R. Soc.
703 A 369, 957-975.
704 Syvitski, J.P.M., Kettner, A.J., Overeem, I., Hutton, E.W.H., Hannon, M.T., Brakenridge,
705 G.R., Day, J., Vorosmarty, C., Saito, Y., Giosan, L., Nicholls, R.J., 2009. Sinking deltas
706 due to human activities. Nat. Geosci. 2, 681-686.
707 Syvitski, J.P.M., Saito, Y., 2007. Morphodynamics of deltas under the influence of humans.
708 Global Planet. Change 57, 261-282.
709 Syvitski, J.P.M., Vörösmarty, C.J., Kettner, A.J., Green, P., 2005. Impact of Humans on the
710 Flux of Terrestrial Sediment to the Global Coastal Ocean. Science 308, 376-380.
711 Tessler, Z.D., Vörösmarty, C.J., Grossberg, M., Gladkova, I., Aizenman, H., Syvitski, J.P.M.,
712 Foufoula-Georgiou, E., 2015. Profiling risk and sustainability in coastal deltas of the world.
713 Science 349, 638-643.
714 Thomas, C.G., Spearman, J.R., Turnbull, M.J., 2002. Historical morphological change in the
715 Mersey Estuary. Cont. Shelf Res. 22, 1775-1794.
716 Tian, B., Zhou, Y., Thom, R.M., Diefenderfer, H.L., Yuan, Q., 2015. Detecting wetland
717 changes in Shanghai, China using FORMOSAT and Landsat TM imagery. J. Hydrol. 529,
718 1-10.
719 van der Wegen, M., Jaffe, B.E., Roelvink, J.A., 2011. Process-based, morphodynamic

720 hindcast of decadal deposition patterns in San Pablo Bay, California, 1856 – 1887. Journal
721 of Geophysical Research: Earth Surface 116, F2008.
722 van Maren, D.S., van Kessel, T., Cronin, K., Sittoni, L., 2015. The impact of channel
723 deepening and dredging on estuarine sediment concentration. Cont. Shelf Res. 95, 1-14.
724 Vörösmarty, C.J., Meybeck, M., Fekete, B., Sharma, K., Green, P., Syvitski, J.P.M., 2003.
725 Anthropogenic sediment retention: major global impact from registered river
726 impoundments. Global Planet. Change 39, 169-190.
727 Walling, D.E., 2006. Human impact on land – ocean sediment transfer by the world's rivers.
728 Geomorphology 79, 192-216.
729 Wang, H., Yang, Z., Saito, Y., Liu, J.P., Sun, X., Wang, Y., 2007. Stepwise decreases of the
730 Huanghe (Yellow River) sediment load (1950 – 2005): Impacts of climate change and
731 human activities. Global Planet. Change 57, 331-354.
732 Wang, J., Baskaran, M., Hou, X., Du, J., Zhang, J., 2017. Historical changes in 239Pu and
733 240Pu sources in sedimentary records in the East China Sea: Implications for provenance
734 and transportation. Earth Planet. Sc. Lett. 466, 32-42.
735 Wang, Z.B., Van Maren, D.S., Ding, P.X., Yang, S.L., Van Prooijen, B.C., De Vet, P.L.M.,
736 Winterwerp, J.C., De Vriend, H.J., Stive, M.J.F., He, Q., 2015. Human impacts on
737 morphodynamic thresholds in estuarine systems. Cont. Shelf Res., R3681.
738 Wei, W., Tang, Z., Dai, Z., Lin, Y., Ge, Z., Gao, J., 2015. Variations in tidal flats of the
739 Changjiang (Yangtze) estuary during 1950s – 2010s: Future crisis and policy implication.
740 Ocean Coast. Manage. 108, 89-96.
741 Wu, Z.Y., Saito, Y., Zhao, D.N., Zhou, J.Q., Cao, Z.Y., Li, S.J., Shang, J.H., Liang, Y.Y.,

742 2016. Impact of human activities on subaqueous topographic change in Lingding Bay of
743 the Pearl River estuary, China, during 1955–2013. Sci. Rep.-UK 6, 37742.
744 Yang, S.L., Belkin, I.M., Belkina, A.I., Zhao, Q.Y., Zhu, J., Ding, P.X., 2003. Delta response
745 to decline in sediment supply from the Yangtze River: evidence of the recent four decades
746 and expectations for the next half-century. Estuarine, Coastal and Shelf Science 57,
747 689-699.
748 Yang, S.L., Milliman, J.D., Li, P., Xu, K., 2011. 50,000 dams later: Erosion of the Yangtze
749 River and its delta. Global Planet. Change 75, 14-20.
750 Yang, S.L., Milliman, J.D., Xu, K.H., Deng, B., Zhang, X.Y., Luo, X.X., 2014. Downstream
751 sedimentary and geomorphic impacts of the Three Gorges Dam on the Yangtze River.
752 Earth-Sci. Rev. 138, 469-486.
753 Yang, S.L., Xu, K.H., Milliman, J.D., Yang, H.F., Wu, C.S., 2015. Decline of Yangtze River
754 water and sediment discharge: Impact from natural and anthropogenic changes. Sci.
755 Rep.-UK 5, 12581.
756 Yun, C., 2004. Recent evolution of Yangtze Estuary and its mechanisms. China Ocean Press,
757 Beijing, China (in Chinese).
758 Zhou, Z., Coco, G., Townend, I., Olabarrieta, M., van der Wegen, M., Gong, Z., D Alpaos, A.,
759 Gao, S., Jaffe, B.E., Gelfenbaum, G., He, Q., Wang, Y., Lanzoni, S., Wang, Z.,
760 Winterwerp, H., Zhang, C., 2017. Is "Morphodynamic Equilibrium" an oxymoron?
761 Earth-Sci. Rev. 165, 257-267.
762 Zhu, L., He, Q., Shen, J., Wang, Y., 2016. The influence of human activities on
763 morphodynamics and alteration of sediment source and sink in the Changjiang Estuary.

764 Geomorphology 273, 52-62.

765

766 **Figure**

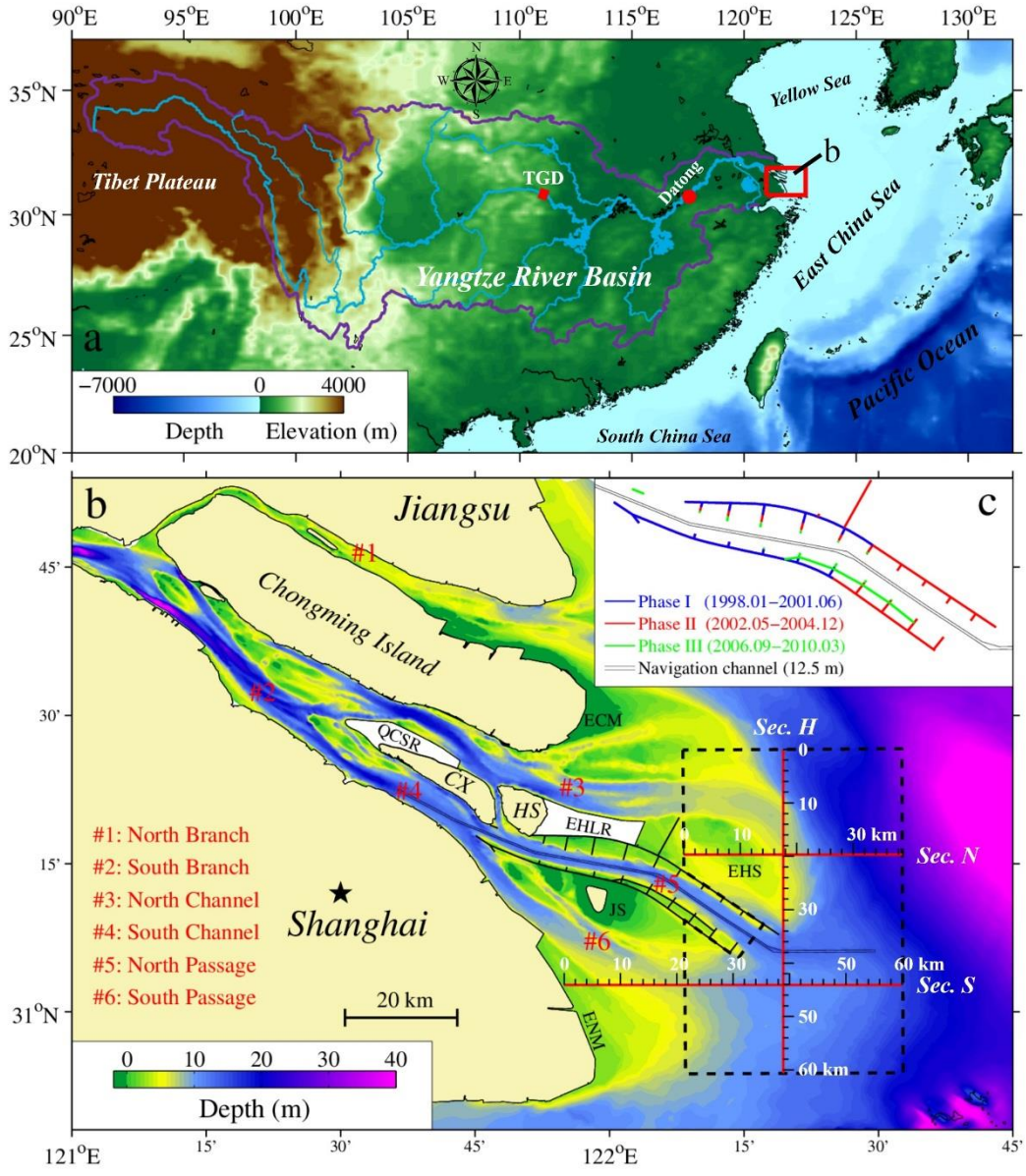

767

768 Fig. 1 (a) Map of the Yangtze River Basin and the location of the Yangtze Estuary (rectangle);

769 (b) the Yangtze Estuary with bathymetry observed in 2010 referred to mean sea level (MSL);

770 (c) the construction phases of the Deep Navigation Channel project. The dashed lines in (b)

771 denote the boundary of the study area, and the ruler lines represent three sections (Sec. N, Sec.

772 S and Sec. H). ECM: East Chongming mudflat; EHS: East Hengsha Shoal; JS: Jiuduansha

773 Shoal; ENM: East Nanhui mudflat; CX: Changxing Island; HS: Hengsha Island; QCSR:

774 Qingcaosha Reservoir; and EHLR: East Hengsha Land Reclamation.

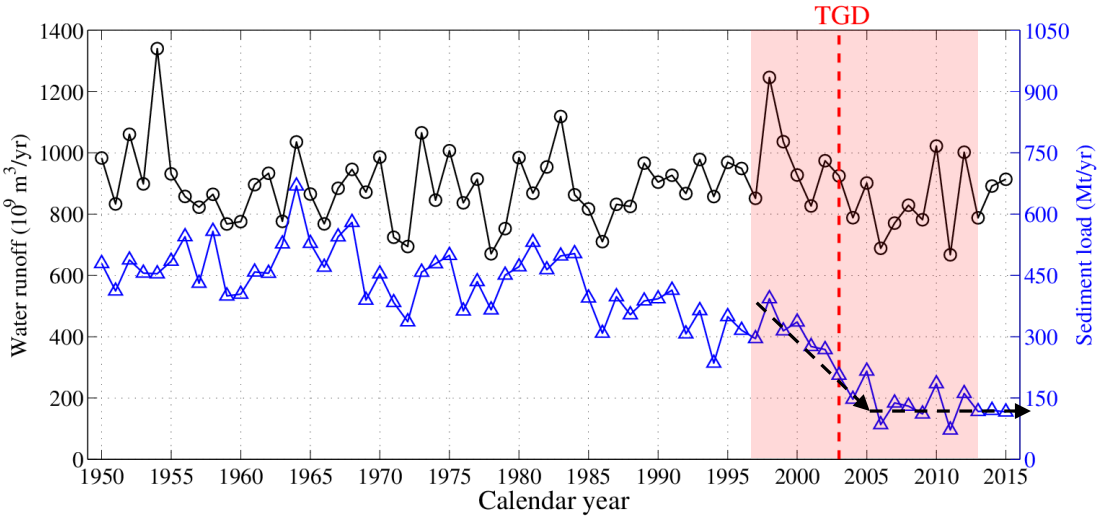

775

776 Fig. 2 Annual river runoff (circles) and suspended sediment load (triangles) since 1950

777 measured at Datong station. The vertical dash line represents the closure of the Three Gorge

778 Dam (TGD) in 2003. The shading area represents the study period 1997-2013.

779

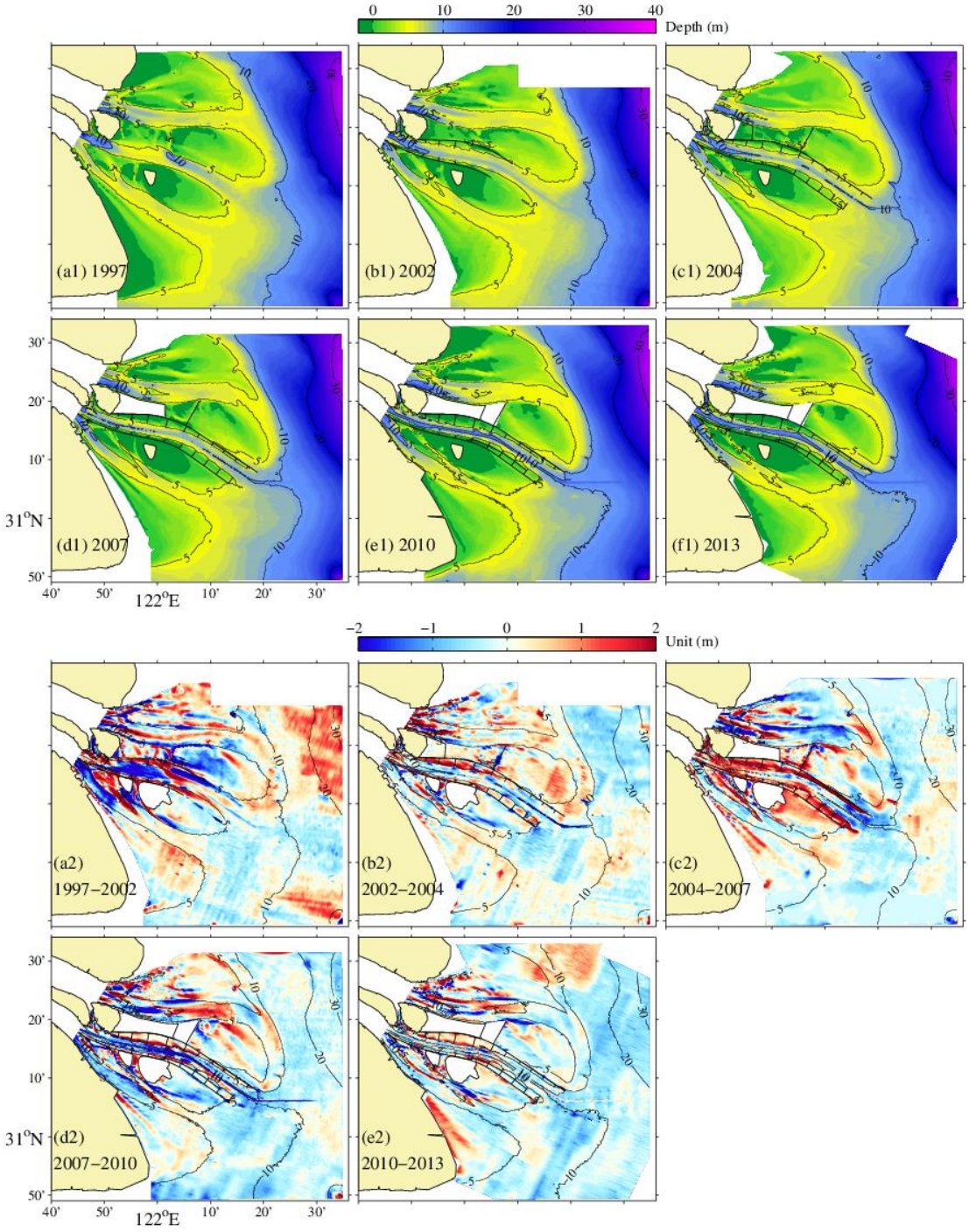

780

781 Fig. 3 Bathymetry (a1-f1) and erosion/deposition patterns (a2-e2) of the Yangtze mouth bar

782 area and adjacent subaqueous delta from 1997 to 2013. The isobaths in the latter year are

783 presented in a2-e2. The water depth and isobaths refer to the theoretical, lowest tidal datum.

784

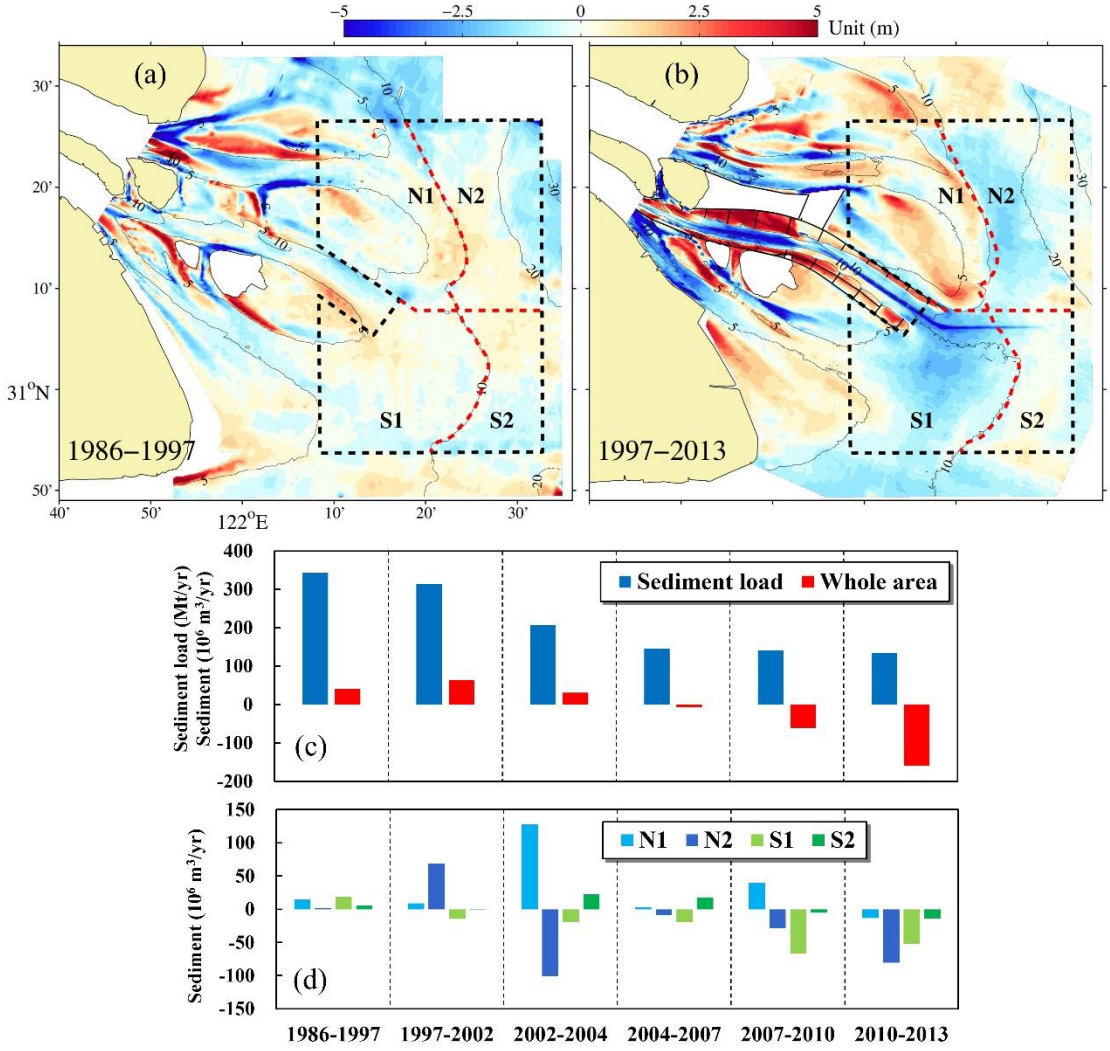

785

786 Fig. 4 (a) Erosion/deposition pattern of the mouth bar area in 1986-1997; (b)
787 Erosion/deposition pattern of the mouth bar area in 1997-2013; (c) Annual-mean sediment
788 load at Datong station and yearly net volume changes of the whole study area and (d) yearly
789 net volume changes of four sub-areas as shown in (a) and (b). The dredged navigation channel
790 is excluded in sediment volume calculations. The red dashed line separating the Area N1 and
791 N2 (also the Area S1 and S2) in (a) and (b) is the 10 m isobath in 1997. The contours in (a)
792 and (b) denote the isobaths in 1997 and 2013, respectively, referring to the theoretical, lowest
793 tidal datum.

794

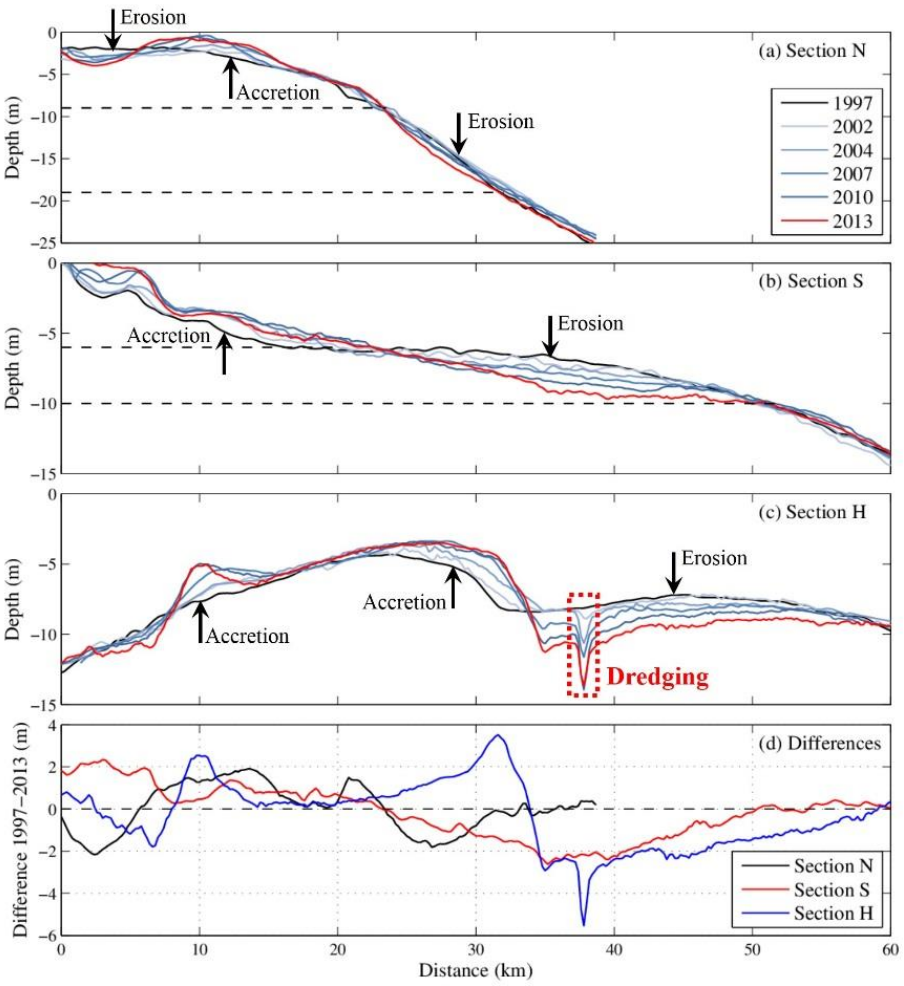

795

796 Fig. 5 Variations of three typical sections from 1997 to 2013 (a, b, c) (heading seaward for the

797 Section N and S and southward for the Section H, see Fig. 1b for the locations) and the

798 differences of the sections between 1997 and 2013 (d) (the water depth refers to the

799 theoretical, lowest tidal datum; positive represents accretion and negative represents erosion).

800

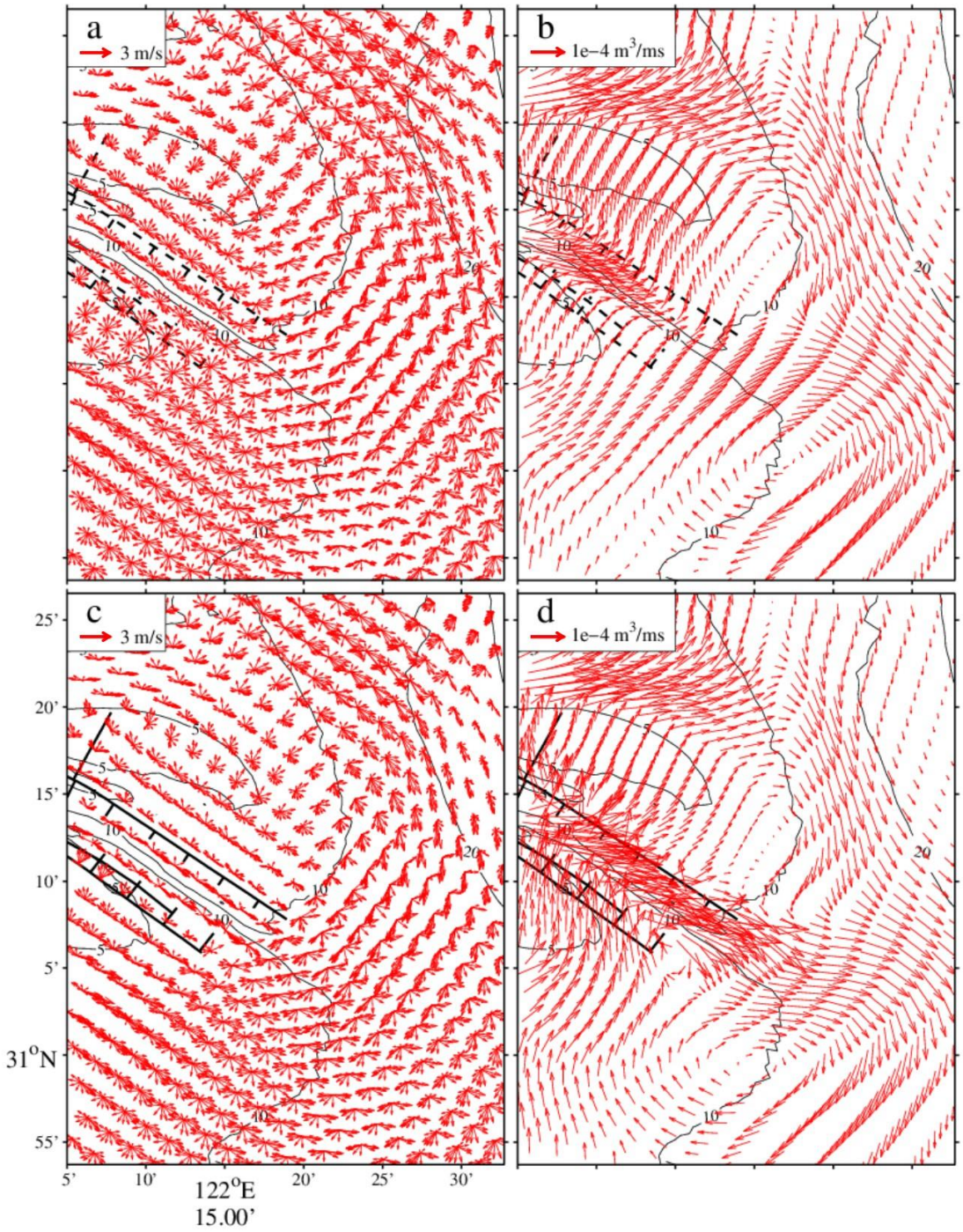

801

802 Fig. 6 Feathers of currents during spring tide (a, c) and monthly-averaged sediment flux (b, d)

803 without (a, b) and with (b, d) training walls. Contours denote the isobaths in 2002 referred to

804 MSL.

805

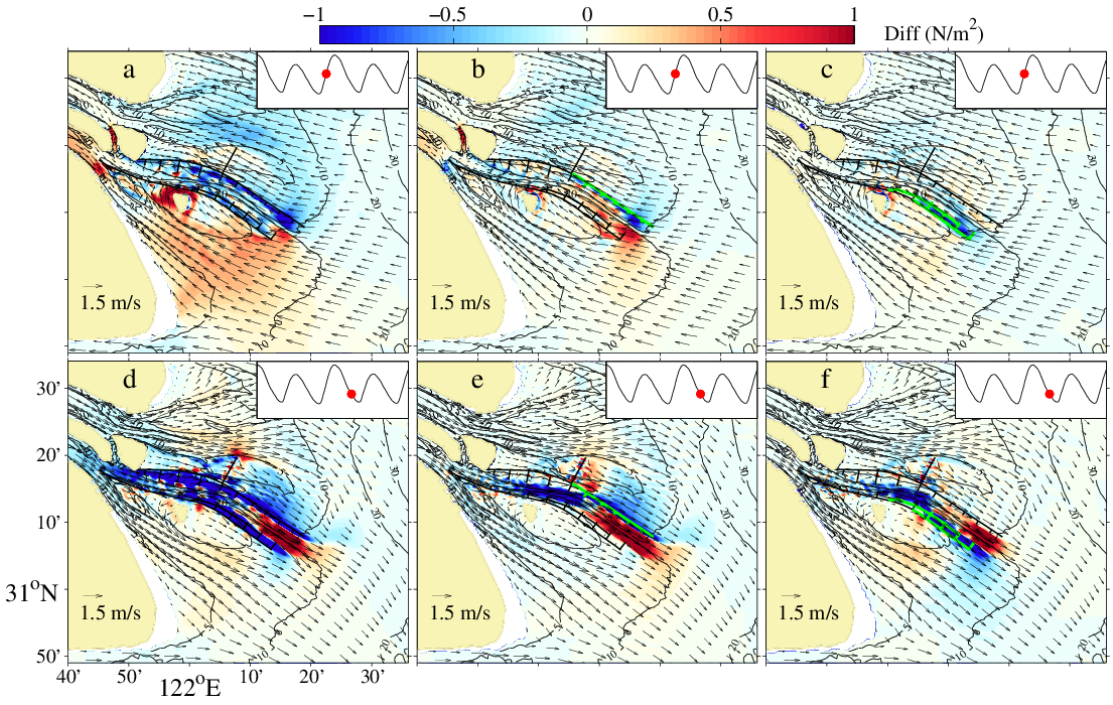

Fig. 7 Tidal currents (arrows) and differences of bed shear stress (background color) between model runs with and without all training walls (a, d), the eastern half of the northern training walls (b, e) and the eastern half of the southern training walls (c, f) (in green color) at flood maximum (a, b, c) and ebb maximum (d, e, f). Contours denote the isobaths in 2002 referred to MSL.

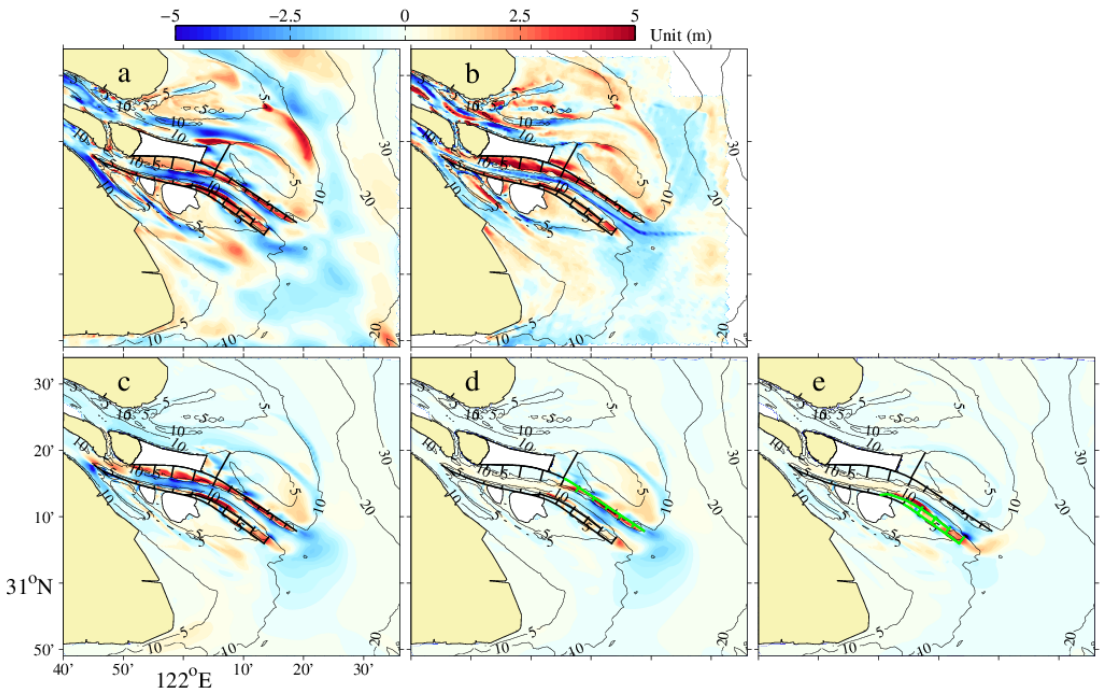

Fig. 8 Modeled (a) and observed (b) erosion/deposition patterns in 2002-2010, and the differences between model runs with and without all training walls (c), the eastern half of the northern training walls (d) and the eastern half of the southern training walls (e) (in green color). Contours denote the isobaths in 2010 referred to MSL.

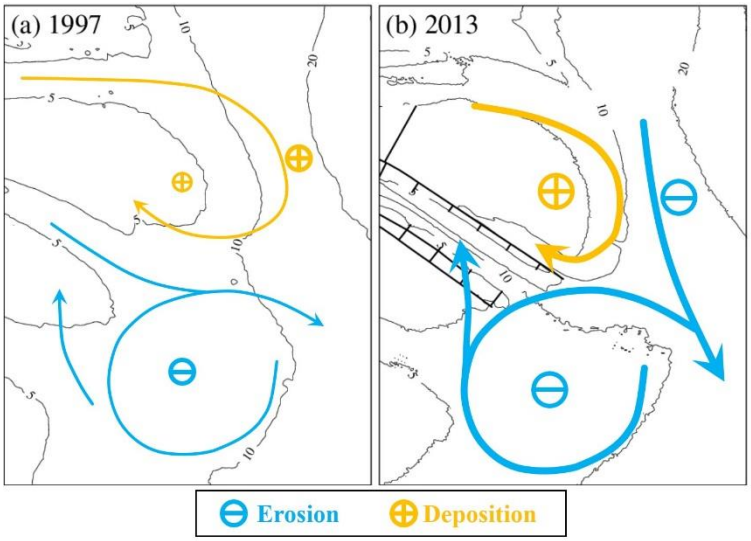

819

820 Fig. 9 Schematized maps of sediment transport paths (arrows) and specific erosion/deposition

821 locations within the study area in 1997 (a) and 2013 (b)

822

Supplementary information for:

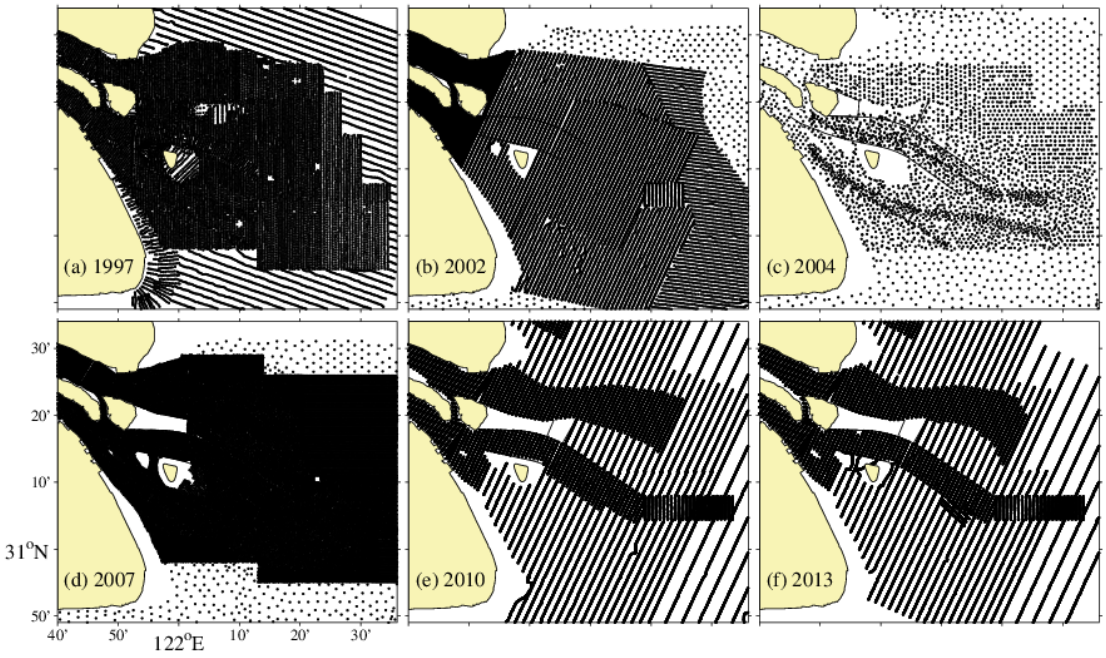

Fig. S1 Bathymetric sample points observed in different years used in this study.

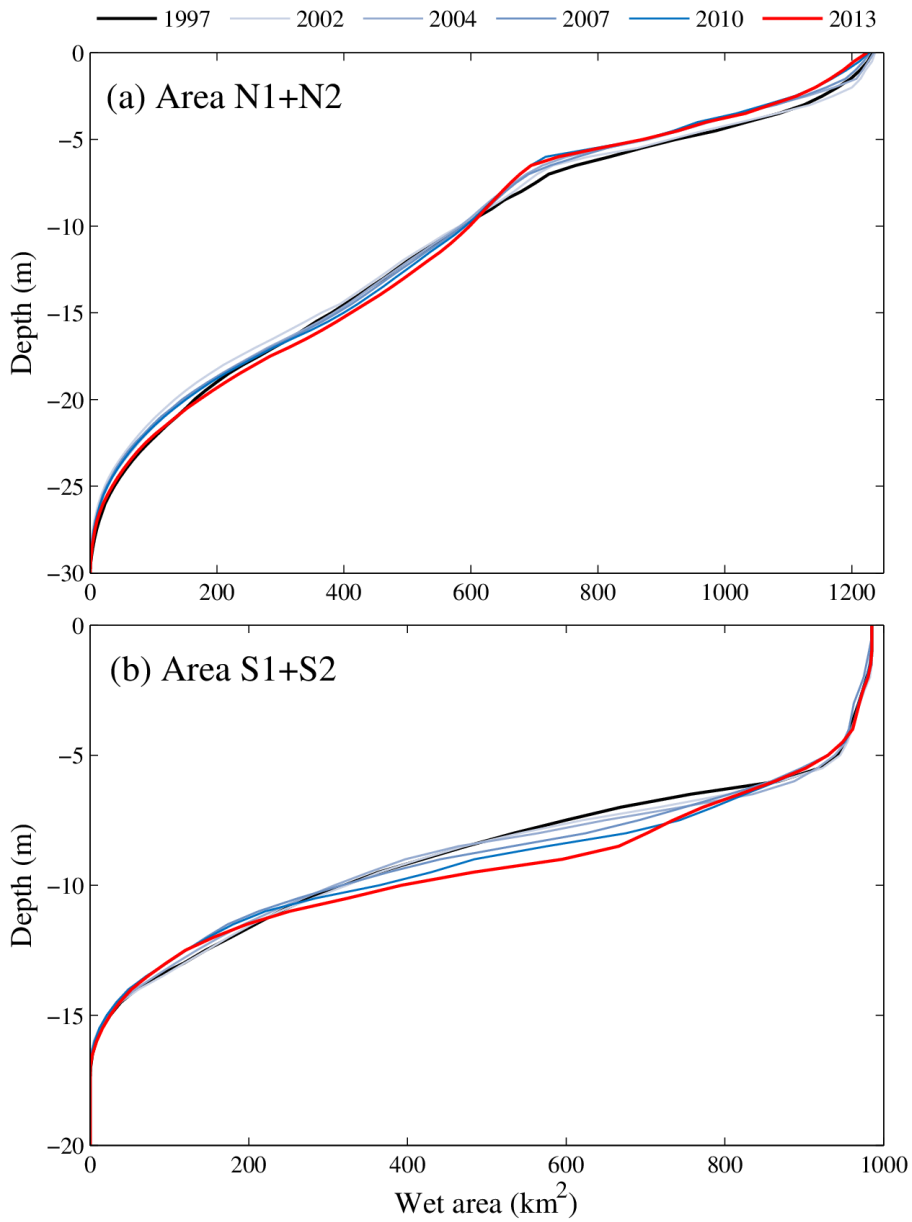

828

829 Fig. S2 Hypsometry curves of the northern part (a) and south part (b) from 1997 to 2013. See

830 Fig. 4a for the domains of the areas.

831

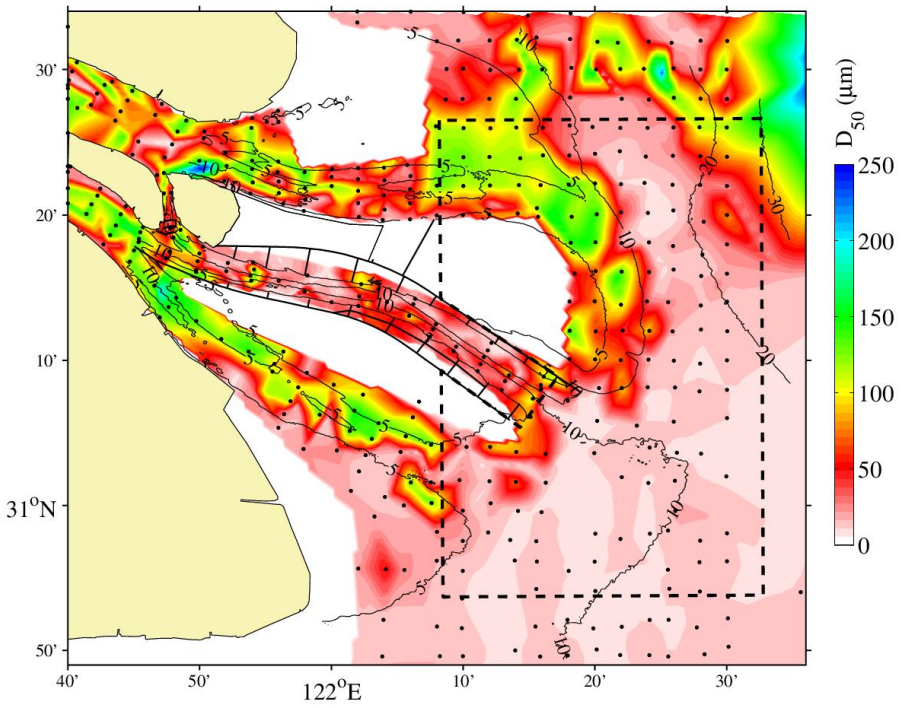

832

833 Fig. S3 Median grain size (D_{50}) at the mouth bar area (black dots denote bed surface sediment

834 samples in September 2015, and dashed line denotes the boundary of the study area as shown

835 in Fig. 1b).

836

837 Tab. S1 Collected bathymetry maps and navigational charts used in this study.

Year	Map Title	Scale	Sources	Survey	Publish
1997	Changjiang Estuary and adjacent area	1:50,000	Yangtze Estuary Waterway Administration Bureau, Ministry of Transport, PRC (YEWAB)	1997	
2002	Changjiang Estuary and adjacent area	1:50,000	YEWAB	2002.12	
	Southern part of Changjiang Estuary	1:130,000	Navigation Guarantee Department of the Chinese Navy Headquarters (NGDCNH)	2001~2002	2002.12
2004	Changjiang Estuary and adjacent area	1:120,000	Maritime Safety Administration, PRC	2004	2004.12
	Jigujiao to Hengsha Island	1:75,000		2004	2005.09
2007	Changjiang Estuary and adjacent area	1:50,000	YEWAB	2007.08	
	Southern part of Changjiang Estuary	1:130,000	NGDCNH	2007~2008	2009.04
2010	Changjiang Estuary and adjacent area	1:50,000	YEWAB	2010.08	
2013	Changjiang Estuary and adjacent area	1:50,000	YEWAB	2013.08	

838

839 Tab. S2 Statistics of the erosion/deposition area and volume and net accretion rate in the
840 whole area and the annual-mean sediment load at Datong Station (Note that the dredged
841 navigation channel is excluded. See Fig. 4a for the domain of the study area. Positive values
842 represent accretion, and negative values represent erosion).

			1986-1997	1997-2002	2002-2004	2004-2007	2007-2010	2010-2013
Sediment load		($Mt\ yr^{-1}$)	**343**	**314**	**207**	**146**	**141**	**134**
Erosion and accretion over the whole study area	Area	(km^2)	2223	2223	2223	2223	2223	2223
	Erosion	Area (%)	33	42	48	54	64	72
		Volume ($10^6\ m^3\ yr^{-1}$)	−30.0	−65.5	−188.5	−134.4	−153.3	−204.2
	Accretion	Area (%)	67	58	52	46	36	28
		Volume ($10^6\ m^3\ yr^{-1}$)	70.6	129.1	219.2	127.4	92.6	44.5
	Net	Volume ($10^6\ m^3\ yr^{-1}$)	**40.6**	**63.6**	**30.7**	**−7.0**	**−60.7**	**−159.6**
		Rate ($mm\ yr^{-1}$)	18.2	28.6	13.8	−3.2	−27.3	−71.8

843

Tab. S3 Statistics of the erosion/deposition area and volume and net accretion rate in the four sub-areas (Note that the dredged navigation channel is excluded. See Fig. 4a for the domains of the sub-areas. Positive values represent accretion, and negative values represent erosion).

			1986-1997	1997-2002	2002-2004	2004-2007	2007-2010	2010-2013
Area N1	Total area	(km^2)	654	654	654	654	654	654
	Erosion	Area (%)	32	39	15	52	39	58
		Volume (10^6 m^3 yr^{-1})	−10.1	−30.2	−9.6	−55.2	−30.4	−37.5
	Accretion	Area (%)	68	61	85	48	61	42
		Volume (10^6 m^3 yr^{-1})	24.7	39.2	137.3	57.9	70.3	24.4
	Net	Volume (10^6 m^3 yr^{-1})	**14.6**	**9.0**	**127.7**	**2.7**	**39.8**	**−13.2**
		Rate (mm yr^{-1})	22.3	13.7	195.2	4.1	60.9	−20.1
Area N2	Total area	(km^2)	584	584	584	584	584	584
	Erosion	Area (%)	44	8	86	57	76	91
		Volume (10^6 m^3 yr^{-1})	−14.3	−2.0	−108.1	−29.2	−36.0	−84.1
	Accretion	Area (%)	56	92	14	43	24	9
		Volume (10^6 m^3 yr^{-1})	16.0	70.6	7.4	20.6	7.2	3.6
	Net	Volume (10^6 m^3 yr^{-1})	**1.8**	**68.6**	**−100.7**	**−8.6**	**−28.8**	**−80.6**
		Rate (mm yr^{-1})	3.0	117.4	−172.5	−14.8	−49.3	−138.0
Area S1	Total area	(km^2)	664	664	664	664	664	664
	Erosion	Area (%)	20	66	53	64	81	69
		Volume (10^6 m^3 yr^{-1})	−2.0	−22.8	−58.7	−46.6	−73.6	−65.8
	Accretion	Area (%)	80	34	47	36	19	31
		Volume (10^6 m^3 yr^{-1})	20.7	8.3	39.8	27.6	7.0	14.0
	Net	Volume (10^6 m^3 yr^{-1})	**18.7**	**−14.5**	**−19.0**	**−19.0**	**−66.6**	**−51.8**
		Rate (mm yr^{-1})	28.1	−21.8	−28.5	−28.6	−100.3	−78.0
Area S2	Total area	(km^2)	321	321	321	321	321	321
	Erosion	Area (%)	41	58	34	29	59	73
		Volume (10^6 m^3 yr^{-1})	−3.7	−10.5	−12.1	−3.4	−13.2	−16.7
	Accretion	Area (%)	59	42	66	71	41	27
		Volume (10^6 m^3 yr^{-1})	9.3	11.0	34.7	21.4	8.1	2.7
	Net	Volume (10^6 m^3 yr^{-1})	**5.5**	**0.5**	**22.6**	**18.0**	**−5.1**	**−14.1**
		Rate (mm yr^{-1})	17.3	1.6	70.4	56.0	−16.0	−43.8